UNIVERSITY OF BIRMINGHAM

An integrated machine learning and metaheuristic approach for advanced packed bed latent heat storage system design and optimization

Anagnostopoulos, Argyrios; Xenitopoulos, Theofilos; Ding, Yulong; Seferlis, Panos

[Link to publication on Research at Birmingham portal](#)

An integrated machine learning and metaheuristic approach for advanced packed bed latent heat storage system design and optimization

Argyrios Anagnostopoulos [a,b,*], Theofilos Xenitopoulos [a], Yulong Ding [c], Panos Seferlis [a]

[a] *Department of Mechanical Engineering, Aristotle University of Thessaloniki, PO Box 454, 54124, Thessaloniki, Greece*
[b] *Institute of Chemistry, University of Silesia, 40-006, Katowice, Poland*
[c] *Birmingham Centre for Energy Storage & School of Chemical Engineering, University of Birmingham, Birmingham, B15 2TT, United Kingdom*

ARTICLE INFO

ABSTRACT

To tackle the challenge of waste heat recovery in the industrial sector, this research presents a novel design and optimization framework for Packed Bed Latent Heat Storage Systems (PBLHS). This features a Deep Learning (DL) model, integrated with metaheuristic algorithms. The DL model was developed to predict PBLHS performance, trained using data generated from a validated Computational Fluid Dynamics (CFD) model. The model exhibited a high performance with an R^2 value of 0.975 and a low Mean Absolute Percentage Error ($<9.14\%$). To enhance the ML model's efficiency and optimized performance, various metaheuristic algorithms were explored. The Harmony Search algorithm emerged as the most effective through an early screening and underwent further refinement. The optimized algorithm demonstrated its capability by rapidly producing designs that showcased an improvement in total efficiency of up to 85% over available optimized experimental PBLHS designs. This research underscores the potential of ML-integrated approaches in laying the groundwork for generalized design frameworks for TES systems, offering efficient and effective solutions for waste heat recovery.

1. Introduction

Core industries are essential for the current global economic structure but represent some of the toughest sectors to sustainably decarbonize [1]. Ambitious goals have been set by the European Union to cut industrial carbon emissions by 42% by 2030 [2]. Based on estimates, the industrial sector consumes 27% of the entire energy and contributes 30% of heat-related CO_2 emissions in the EU [3]. Notably, 70% of the energy need stems from thermal processes in industries, making up 18.9% of the total EU energy demand [4]. These processes release vast amounts of waste heat, with roughly 400 TWh/year or one-fifth being of high-grade quality, which translates to good recovery and reuse potential [5].

Consequently, waste heat recovery (WHR) stands out as an emerging solution for energy-intensive sectors [6]. Among various WHR techniques, thermal energy storage (TES) is promising in bridging the gap between waste heat generation and subsequent consumption needs [7]. TES efficiently tackles the spatial and temporal discrepancies observed in methods like heat pipes, recuperators and regenerators. Its adaptive framework fine-tunes process parameters to enhance output efficiency, curbing losses associated with startups and partial operations [7]. Such a

design proves advantageous in terms of capital costs, especially when contrasted with other WHR technologies like Organic Rankine Cycle systems or thermoelectric generators [8].

TES is primarily categorized into sensible, latent, and thermochemical; the latter remains in its developmental phase, mostly focused on materials-level research [9]. Sensible TES (STES) stands as a time-tested technology, boasting a history spanning centuries [9]. It leverages affordable, reliable and stable performance. However, its drawbacks include a rapid decline in temperature during its heat release phase (discharge) and a relatively low energy density [9]. On the other hand, Latent Heat TES (LHTES) is based on the capability of a substance, commonly known as a phase change material (PCM), to absorb or dispel heat at a constant temperature during its phase transition. Its potential has garnered immense research focus lately, with significant applications emerging in fields like solar energy harnessing, peak power and WHR [10]. LHTES showcases limited temperature variation through its charge/discharge phases and an energy density that surpasses that of STES [10]. Yet, PCMs come with challenges: they exhibit subpar thermal conductivity, subcooling, susceptibility to corrosion and an often large change in volume during phase transition [11]. These challenges impact the efficiency of LHTES on individual devices as well as on a system

---

level. Addressing these challenges is feasible by integrating them within a porous framework predominantly made up of heat-resistant substances (i.e. refractory materials) [12,13]. The resulting material is termed as a Composite Phase Change Material (CPCM). Beyond their application in LHTES, CPCMs are also fit for combined STES-LHTES configurations. These integrated TES systems have been identified as highly promising future solutions [14].

PCM encapsulation significantly boosts charging/discharging efficiency [11]. CPCMs resolve the issue of PCM leakage, improve PCM handling and compatibility and increase their heat transfer area. Moreover, they enable PCM deployment in direct heat transfer systems [15]. These systems often have reduced thermal resistance due to eliminating an intermediary heat exchanger, leading to superior heat transfer [14]. Furthermore, with the heat transfer fluid (HTF) serving as the storage medium, storage tank designs can capitalize on beneficial thermal stratification, enhancing the overall system's efficiency [14]. This enhancement, in turn, amplifies the system's exergy, especially during dormant periods [16]. Direct systems often consist of fewer components than their indirect counterparts, resulting in a more economical capital investment [17].

A notable example of an indirect TES system is the packed bed. When packed beds integrate CPCMs, they are termed as packed bed latent heat storage systems (PBLHS). PBLHS present a straightforward and effective technology suitable for diverse temperature ranges. This flexibility allows for its integration with both high-temperature applications like small concentrated solar power plants (CSP) or waste heat emissions from steel manufacturing processes, and low-temperature applications, such as solar thermal systems or waste heat streams [16]. The extensive application scope, overall efficiency, and cost-effective setup of PBLHS have drawn increasing interest in this technology [18].

PBLHS research traces back to the late 1980s. Ananthanarayanan and colleagues formulated a computational model to forecast heat exchange within a packed bed containing encapsulated Al–Si PCMs, streamlining its application as an almost-isothermal heat recuperator [19]. Concurrently, Beasley and Ramanarayanan conducted experimental studies on a PBLHS that featured a bed with encapsulated paraffin wax. Their research delved into the effective heat transfer coefficient across various Reynolds numbers [20]. Additionally, in that period, Yagi and Akiyama undertook initial experiments on PBLHS utilizing encapsulated metals, targeting waste heat recovery tasks at 500K [21].

Fast-forwarding to more recent times, an interesting theoretical exploration by Wu et al. revolved around cascaded PBLHS designs. The study identified that systems incorporating numerous cascaded PCMs have improved charging efficiency. In another work, Liu et al. explored 3D modelling of PBLHS, highlighting the pivotal influence of radial porosity on heat transfer and PCM melting time. The authors further showcased that aspect ratio optimization can improve system performance [22]. Grabo et al. investigated a PBLHS with non-spherical capsule designs using a validated CFD model. These geometries offered up to a 20% increase in storage capacity and a reasonable thermal power output of approximately 4 kW [23]. Wang et al. developed a transient two-dimensional dispersion-concentric model to model a PBLHS. Results show that radial gradient arrangement significantly enhances heat transfer performance and reduces system pressure drop with a maximum overall energy efficiency of 84.16% [24]. Dong et al. proposed a novel PBLHS design with a biomimetic vein hierarchical structure. The latter improved temperature distribution, heat transfer area, and thermal response compared to the conventional uniform structure [25]. Nekoonam and Ghasempour, using a 2D model and employing a Genetic Algorithm, optimized the thermal conductivity of PCMs in solar-integrated PBLHS designs. They maximised the stored energy by tuning inlet temperature and flow rate [26]. El Sihy et al. investigated numerically a PBLHS in terms of the number of PCMs and their arrangement, latent heat, and capsule size with respect to system performance. Their results highlighted improved performance with

certain PCM configurations, a significant impact of latent heat, and superior behaviour with smaller capsule sizes [27]. Manente et al. developed an algorithm to enhance heat recovery from a steel industry's flue gas stream, focusing on steam or electricity production. They found that a PBLHS, in combination with organic Rankine or Kalina cycles, produced the most steam and electricity. Investment had a payback period of seven years, making it more profitable than high-cost tank-based storage units [28]. Wu et al. adeptly utilized CFD to evaluate the effect of various parameters on the performance of a PBLHS and noted the effect of inlet velocity and temperature [29]. Alptekin and Ezan used an in-house 1D transient model to study a latent heat TES unit in Izmir, Turkey. They determined optimized HTF flow rates and capsule sizes for better efficiency under varying solar conditions. Integrating a heat pump and specific PCM types further enhanced performance [30]. He et al. employed a lab-built platform and a one-dimensional transient model to optimize a two-layered packed-bed heat storage (OT-PTES) system. They highlighted key factors like capsule size, PCM melting temperature difference, and volume ratio, achieving enhanced charging and discharging efficiencies in their design [31]. Mao and Cao employed a 3D concentric-dispersion model to investigate the influence of capsule sizes in three-layered packed beds for optimizing CSP plants. Their study demonstrated that varying capsule geometries significantly impacted heat transfer and thermal performance [32]. Mohammadnejad and Hossainpour employed Comsol multi-physics for a CFD study on packed beds with encapsulated PCMs. Exploring layer configurations and porosity, they identified setups improving performance by 29.2% [33]. Zhang et al. used the finite volume method (FVM) to study cascaded latent heat storage packed beds with varied capsule diameters. They found variable diameter capsules improved heat and exergy storage capacities by up to 10.68% compared to equal diameters [34]. Aziz et al. applied the effectiveness-number of transfer units (ε-NTU) method to optimize a packed-bed system with spherical PCMs. By varying parameters like tank dimensions and sphere counts and sizes, they pinpointed configurations maximizing energy storage effectiveness [35]. A recent review of PBLHS was conducted by He et al. The authors delved into design optimization, capsule shapes, packing methods, and operational strategies [18].

Conclusively, a thorough review of relevant literature reveals that the majority of research conducted on PBLHS modelling involves classical finite element models (FEM) or analytical models. The prevalent use of FEM in PBLHS research, while precise, presents limitations such as computational expense and time-intensiveness, restricting their utility in expansive, real-time applications. Additionally, FEM's adaptability is constrained, often necessitating extensive modification to fit varying operational scenarios. Conversely, analytical models offer flexibility but at the cost of precision, as they rely on assumptions that may not align with the complexities of actual conditions.

Machine learning (ML), emerging as a compelling alternative, mitigates these issues with its ability to handle large datasets and with greatercomputational efficiency, providing a balanced approach to accuracy and computational demand in TES system modeling. ML has shown great potential in solving intricate problems across diverse domains [36]. When compared to FEM and analytical models, ML has considerably lower computational requirements, with no substantial trade-off in accuracy, resulting in a more efficient solution-providing approach [37]. This is because unlike FEM and analytical models, AI operates with approximate models, delivering solutions through near-accurate reasoning. Despite this it is able to properly manage uncertainty and imprecision [16]. This is due to the rise of more robust computing resources, and advancements in algorithms and techniques for data analysis.

These features have made ML a pretty promising approach for TES modelling. Numerous studies have emerged in solar collectors [38], air conditioning [39], TES material discovery [40], concentrated solar power [41] and space heating among [42] others. In a study conducted by Ermis et al., they explored the performance of a finned-tube LTES

system that utilized ice as a PCM. They found that ML was able to better predict the performance compared to traditional modelling methods and linear and polynomial fitting techniques [43]. In another work, Hofmann et al. modelled the performance of a packed bed regenerator using both a 1-D model and a grey-box model reinforced by ML. They demonstrated that while the traditional 1D physical model is robust, the ML model offers significant advantages in terms of efficiency and adaptability, especially when ample data is available [44]. A recent thorough review for ML applications in TES has been conducted by He et al. [37].

In terms of PBLHS, two very recent works have employed ML to predict performance. The first one is that of Li and Lv [45]. The authors used Latin Hypercube Sampling (LHS) and numerical simulations to generate a training dataset. They then employed the Light Boosting Machine (LGBM) method to analyze the impact of key factors on PBTESS performance. Their findings highlighted the significance of parameters like HTF flow rate, tank dimensions, and PCM phase change temperature on various performance metrics. Post-optimization using the naive Bayes algorithm, they observed substantial improvements in heat release time, heat storage, and material utilization rates. However, despite significantly improving heat metrics, the study had limitations. It only assessed an inlet heat stream range of 100 °C and a single order of magnitude for the inlet flow rate. Additionally, the research didn't incorporate a cascade system, well known for enhancing TES performance [46]. Anand et al. conducted the second work, which evaluated various ML models, including LR, SVR, KNN, DT, RF, and XGB, to assess a PBLHS system's performance, particularly its charging and discharging times. They found the XGB model resulted in the highest R^2 value of 0.982 and the lowest error metrics. The study also delved into the impact of various thermo-physical properties and operating parameters on the system's performance. For instance, changes in thermal conductivity, latent heat, and density significantly influenced charging and discharging times. However, while the study showcased the potential of data-driven approaches in PBTES performance analysis, there were notable limitations. A notable concern was overfitting, exacerbated by the use of a narrow data range with excessively high resolution, such as second-digit temperature accuracy. This approach not only posed overfitting risks but also impacted data quality, as high-resolution data can overlap with measurement errors. Consequently, this led to increased computational demands due to the need for processing a large number of data points, affecting the overall efficiency of the model training process. Additionally, the study's scope was limited to a 25–100 °C temperature range, and extrapolation beyond this could be problematic. Notably, this work also did not employ a cascade system. In summary, while the current research offers valuable insights into PBLHS system analysis using ML models, it's essential to consider its limitations and the context in which the models are applied [45].

Conclusively, in the face of rising industrial carbon emissions, WHR emerges as a crucial solution. TES, and especially LHTES, offers a promising avenue. While PCMs have their challenges, encapsulation techniques have led to enhanced efficiency and performance in PBLHS. Traditional modelling of PBLHS, such as finite element models, has its limitations. ML presents a promising alternative, as evidenced by recent studies. However, current ML research on PBLHS is narrow in scope, often missing out on broader temperature ranges and cascade systems. In conclusion, while PBLHS holds significant potential for wWHR, expanding ML-integrated research is pressing to harness its capabilities. Building on the identified research gap, this study explores a cascade PBLHS using advanced deep learning ML methods. This investigation is distinct from prior research and encompasses more advanced techniques and an extensive temperature and flow rate spectrum. Moreover, it incorporates dynamic properties of PCMs based on their specific melting points. This approach offers a comprehensive and realistic design solution for TES systems, poised to advance the current state-of-the-art significantly.

2. Methods

2.1. Model definition

The modelling analysis utilized the computational fluid dynamics (CFD) platform, COMSOL Multiphysics.

Pertaining to the model, several foundational assumptions were incorporated. First, the domain packed with PCM capsules is treated as a continuous, unified, and isotropic porous environment. Second, any radiation-driven heat transfer within the tank is overlooked, and no intrinsic heat sources are present. Third, fluid dynamics within the tank are presumed stable, with no mass deposition or generation occurring. Fourth, the potential thermal expansion effects of the CPCM or the tank's materials aren't taken into account. For the solid walls interfacing with the fluid domain, a "no-slip" condition was applied, ensuring zero fluid velocity at these boundaries. Similarly, the standard no-slip formulation was adopted within the porous medium, treating the solid matrix as impermeable barriers where fluid cannot slip.

The "Free and Porous Media Flow" interface is employed to compute fluid dynamics within the packed bed, utilizing the Navier-Stokes equation for compressible flow. The momentum equation was represented as:

$$\frac{1}{\varepsilon_p}\rho(u \cdot \nabla)u = \nabla \cdot (-pI + K) - \left(\mu\kappa^{-1} + \beta\rho|u| + \frac{Q_m}{\varepsilon_p{}^2}\right)u + F \tag{1}$$

Where, ε_p is the porosity (dimensionless), ρ denotes fluid density (kg/m^3), u is the fluid velocity (m/s), and ∇ is the gradient operator, p stands for fluid pressure (Pa), I is the identity matrix, K accounts for external force effects, μ represents dynamic viscosity (Pa·s), κ indicates the permeability of the porous medium (m^2), β is a drag coefficient (dimensionless), Q_m refers to the source term (kg/m^3·s for the mass source; W/m^3 for the heat source), and F is the volume force (N/m^3).

Given the conditions of high Reynolds number (Re > 10) or elevated Knudsen numbers (Kn > 0.1), typical of packed bed flow, Darcy's law was deemed unsuitable. Therefore, the non-Darcian flow model, relying on the Ergun equation, is employed, for which the drag coefficient and permeability are defined as:

$$\beta = \frac{1.75}{d_p\left(\varepsilon_p{}^3\right)} \frac{\left(1 - \varepsilon_p\right)}{\varepsilon_p{}^3} \tag{2}$$

And

$$k = \frac{d_p{}^2}{150} \frac{\varepsilon_p{}^3}{\left(1 - \varepsilon_p\right)^2} \tag{3}$$

The mass conservation/continuity is expressed as:

$$\rho \cdot \nabla \cdot u = Q_m \tag{4}$$

At the inlet, measures were taken to ensure that the fluid entered the domain without any sideways or tangential flow; all fluid flow was directed perpendicularly to the inlet boundary. The total volumetric flow rate was established based on integration over the inlet boundary, considering the radial position and the normal component of flow velocity at each point. For the outlet conditions, the boundary stress was regulated to ensure a controlled exit of the fluid. Additionally, a mechanism was in place at the outlet to suppress any backflow, maintaining the outlet pressure above ambient value. In the simulation, gravity was explicitly modelled with a direction opposite to the charging flow. Furthermore, the Boussinesq approximation was employed to efficiently simulate thermal convection.

The thermal dynamics within the packed bed were simulated using the "Heat Transfer in Solids and Fluids" interface in COMSOL Multiphysics. The equation was expressed as:

$$\rho C_p u \cdot \nabla T + \nabla \cdot q = Q \tag{5}$$

Where C_p represents the specific heat capacity at constant pressure (J/(kg·K)) T is the temperature (K), q stands for the heat flux (W/m^2), which is defined through the relation q = $- k\nabla$T, where k is the thermal conductivity(W/(m·K)). Finally, Q is a volumetric heat source(W/m^3).

For the fluid domain, the equation is the same as Eq. (5) but also includes a term for heat source due to viscous dissipation (Q_{vd}) after Q. The air density is modelled according to the ideal gas equation. A linear discretization scheme was chosen to solve the above equations, ensuring numerical stability and precision.

A Local Thermal Nonequilibrium (LTNE) approach was employed to accurately account for potential temperature disparities between the fluid and solid phases within the porous medium. The heat transfer in the fluid phase within the porous medium is represented by:

$$\rho_f C_{p,f} u \cdot \nabla T_f + \nabla \cdot q_f = Q_{s,f} + \varepsilon_p Q_f + \varepsilon_p Q_p + \varepsilon_p Q_{vd} \qquad (6)$$

Where

$$q_f = - \left(\varepsilon_p k_f + k_{disp} \right) \nabla T_f \qquad (7)$$

Where f denotes the fluid phase and $disp$ the dispersion.

The heat transfer in the solid phase (CPCM) is expressed as:

$$\nabla \cdot q_s = -Q_{s,f} + \theta_s Q_s \qquad (8)$$

Where s denotes the solid phase

The heat exchange term between the fluid and solid phases is given by:

$$Q_{s,f} = S_b h_{sf} \left(T_s - T_f \right) \qquad (9)$$

With the specific surface area S_b defined as

$$S_b = \frac{6\theta_s}{d_{pe}} \qquad (10)$$

Where d_{pe} is the diameter of the spherical CPCMs in the packed bed in (m)

And the heat transfer coefficient h_{sf} defined as:

$$h_{sf} = \left[d_{pe} \left(\frac{1}{k_f Nu} + \frac{1}{k_s} \right) \right]^{-1} \qquad (11)$$

Where Nu is the Nussel number.

The properties of the CPCM and its phase change were modelled using the following relationships:

An average value for each phase defines the density of the CPCM.

The specific heat capacity of the solid CPCM $C_{p,s}$ is represented by:

$$C_{p,s} = \theta_1 C_{p,1} + \theta_2 C_{p,2} + L_{1\rightarrow2} \frac{\partial a_m}{\partial T} \qquad (12)$$

Where θ_1 and θ_2 are the volume fractions of the two phases of the CPCM (solid and liquid),

$C_{p,1}$ and $C_{p,2}$ are the are the specific heat capacities of the two phases, $L_{1\rightarrow2}$ is the latent heat associated with the phase transition from phase 1 to phase 2, and a_m is the mean volume fraction, given by:

$$a_m = \frac{1}{2} \frac{\theta_2 - \theta_1}{\theta_1 + \theta_2} \qquad (13)$$

The thermal conductivity of the CPCM, is described as:

$$k_s = \theta_1 k_1 + \theta_2 k_2 \qquad (14)$$

At the tank inflow, the heat flux is determined by the enthalpy change from a reference state. This enthalpy change, represented by ΔH, is determined by integrating the specific heat at constant pressure over the temperature range from a reference ambient temperature to the local inlet temperature.

The losses from the side of the tank are modelled as a specific heat flux q_0 across the boundary defined as:

$$q_0 = h \left(T_{amb} - T \right) \qquad (15)$$

Where T_{amb} is the ambient temperature, and h, is the heat transfer coefficient between the tank and the ambient surroundings determined from an experimental formula [47].

The problem-solving methodology involves first addressing the free porous media flow in a stationary phase, decoupling the flow from heat transfer to ensure robust initial conditions. Subsequently, heat transfer dynamics in solids and fluids are solved in a time-dependent phase, incorporating non-isothermal flow effects. To solve the presented problem, the Parallel Direct Solver (PARDISO) is employed, tailored for efficiently handling large sparse matrices typical of finite element analyses. The solver settings were optimized with automatic preordering and scheduling methods to improve computational efficiency, leveraging techniques such as row preordering, reuse of preordering, Bunch-Kaufman pivoting, and multithreading for forward and backward substitution. The solver was set with a relative tolerance of 0.0001 to ensure numerical accuracy. For the time-dependent step, a timestep of 0.5 min was used to adequately capture the system's transient behaviour.

Given these considerations, the tank's structure is interpreted as axisymmetric, enabling the packed-bed region's representation as a porous environment with radial variations in porosity. The entire tank is streamlined into a two-dimensional axi-symmetric model for simulation to enhance computational efficiency.

The total heat stored within the TES tank is ascertained based on the heat transferred to TES tank during the charging processes. Specifically, the heat contribution by air (heat transfer fluid) is expressed as:

$$Q_{charge} = \dot{m}_{air} \times \tau \times \sum_{n=1}^{N} \left(T_{inlet} C_{p,air,inlet} - T_{outlet} C_{p,air,outlet} \right) \qquad (16)$$

Where m_{air} represents the mass flow rate of the air (kg/s), τ the timestep of the simulation (s) and inlet and outlet denote the entrance and exit of the TES tank. For the discharging process this is:

$$Q_{discharge} = \dot{m}_{air} \times \tau \times \sum_{n=1}^{N} \left(T_{outlet} C_{p,air,outlet} - T_{inlet} C_{p,air,inlet} \right) \qquad (17)$$

It should be noted that the value of the C_p of the air is adjusted based on the temperature using linear fittings available in the COMSOL Material's Library.

The charging (η_{ch}) and discharging efficiency (η_{dis}) of the PBLHS is then denoted as:

$$\eta_{ch} = \frac{Q_{charge}}{Q_{in}} \qquad (18)$$

and

$$\eta_{dis} = \frac{Q_{discharge}}{Q_{max}} \qquad (19)$$

Where Q_{max} is the maximum theoretical energy that can be captured by the PBLHS. This encompasses three components: the energy retained by the CPCM, the energy retained by the carbon steel tank, and the energy retained by the HTF. Consequently, it can described as:

$$Q_{max} = Q_{tank} + Q_{HTF} + Q_{CPCM} \qquad (20)$$

The energy retained by the tank, HTF and CPCM is then expressed respectively as:

$$Q_{tank} = m_{steel} C_{p,steel} \left(T_{entry,avg} - T_{init} \right) \qquad (21)$$

and

$$Q_{HTF} = V_{flow} \rho_{flow} C_{p,flow} \left(T_{entry,avg} - T_{init} \right) \qquad (22)$$

and

$$Q_{\mathrm{CPCM}} = m_{\mathrm{CPCM}} C_{p,solid} \left(T_{entry,avg} - T_m \right) + m_{\mathrm{CPCM}} h_t + m_{\mathrm{CPCM}} C_{p,liquid} \left(T_m - T_{\mathrm{CPCM,final}} \right) \tag{23}$$

Where, m_{steel} and m_{CPCM} is the total mass of the steel and CPCM, respectively; T_{init} denoted the initial temperature; V_{flow} the flowrate of air; ρ_{flow} the density of air; T_m, and $T_{\mathrm{CPCM,final}}$, denote the melting point temperature and the final temperature of the CPCM, respectively. $C_{p,solid}$ and $C_{p,liquid}$ denote the specific heat capacities of the solid and liquid phases of the CPCM, respectively, while $C_{p,\mathrm{steel}}$ stands for the specific heat capacity of stainless steel; h_t the latent heat during solid liquid phase transition.

The thermophysical properties of the CPCM are obtained from literature studies. These of air are obtained as a function of temperature through correlations provided in the literature that match the operating conditions of the PBLHS presented here [48]. These are:

For the density:

$$\rho_f \left(\mathrm{kg/m^3} \right) = 7.487 \times 10^{-7} T_f^6 - 2.68 \times 10^{-13} T_f^5 + 3.898 \times 10^{-10} T_f^4 - 3.025 \times 10^{-7} T_f^3 + 0.0001421 T_f^2 - 0.04642 T_f + 12.81 \tag{24}$$

And for the specific heat capacity under constant pressure,

$$c_{pf} (\mathrm{J/kgK}) = 3.756 \times 10^{-10} T_f^4 - 1.042 \times 10^{-6} T_f^3 + 0.0009458 T_f^2 - 0.1178 T_f + 1023 \tag{25}$$

The total efficiency (η_{total}) of the PBLHS is then determined as follows:

$$\eta_{\mathrm{total}} = \eta_{\mathrm{ch}} \cdot \eta_{\mathrm{dis}} \tag{26}$$

2.2. Data generation

An extended database is required to obtain a generalized ML-based model that can predict the design and performance of a PBLHS system. To this end, a large-scale parametric analysis was conducted using the model described in the previous section. The investigated parameters are reported in Table 1. These involve all the important parameters when designing a PBLHS system for TES/WHR. These range from geometrical ones like aspect ratio and insulation thickness to material ones such as the CPCM particle size or its thermal properties.

One innovation of this work, as opposed to the previously reported in

Table 1
Evaluated variables in the deep learning model.

Variable Description	Symbol	Units	Lower Bound	Upper Bound
Storage Tank Diameter	ds	m	0.15	6
Inlet Diameter	din	m	0.1	2
Particle Radius	dp	m	0.01	0.25
Inlet Volumetric Flowrate	V_in	m³/s	0.1	6
Insulation Thickness	s_ins	m	0.01	1
Storage Tank 1 Length	L1	m	0.1	5
Storage Tank 2 Length	L2	m	0.1	5
Storage Tank 3 Length	L3	m	0.1	5
Charging Time	t_charging	h	1	8
Discharge Time	t_discharge	h	1	28
Initial Temperature	T0	°C	−5	30
External Temperature	T ext	°C	−5	30
Melting Point of CPCM1	T_m1	°C	0.1	550
Melting Point of CPCM2	T_m2	°C	0.1	500
Melting Point of CPCM3	T_m3	°C	0.1	500
Upstream Temperature	Tu	°C	0.1	650

Table 2
PCMs selected for the data generation process and reference for their properties.

Phase Change Material type	Temperature (°C)	Reference
Paraffin RT Series	50–100	Company website
LiNO₃–NaNO₃–KNO₃–Ca(NO₃)₂	98–147	[49–51]
NaNO₂–KNO₃	138–220	[51–53]
NaNO₃–KNO₃	220–334	[51,54–56]
Li₂CO₃–Na₂CO₃–K₂CO₃	397–600	[57,58]

the literature, is that the system is treated as a cascade with 3 CPCMs. Since the inlet of the system is at the top of the tank, the melting point of these CPCMs is selected sequentially from highest (top layer) to lowest (bottom layer). A temperature constrain was placed (<600 °C) so that the operating temperatures are in a range where PCMs are typically chemically stable.

A critical aspect of PBLHS optimization involves tailoring the melting point of PCMs to match the specific requirements of the particular waste heat stream. However, selecting a PCM with an optimal melting point for a given temperature range inherently involves choosing a material with a distinct specific heat capacity (C_p). The variability of PCM C_p with respect to melting point is visualized in Fig. 1.

This variability in C_p is crucial, as different materials—each with certain values—are required to optimally cover the extensive temperature range of 25 °C–600 °C. To accurately account for these changes the material properties are incorporated in this model as a function of their melting point. This approach ensures that the generated dataset reflects the real-world performance of PCMs across the targeted temperature spectrum.

In the case of C_p to account for the variations resulting from different PCM compositions, the mixing theory is employed. Using the mixing theory the effective C_p of CPCMs can be calculated by considering the contributions of each component material. The equation used in this theory is as follows:
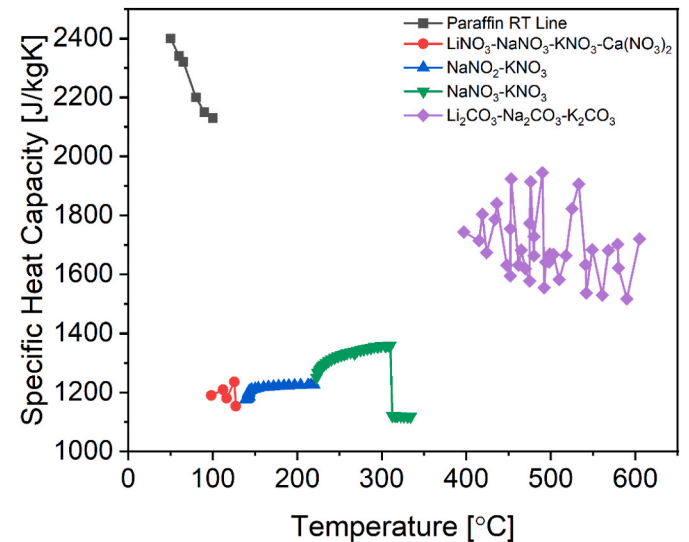

Fig. 1. Variation of specific heat capacity with temperature for different PCMs selected for data generation process. Reference for their properties are in Table 2.

$$C_p^{CPCM} = \sum \left(x_i \cdot C_{p,i} \right) \tag{27}$$

Where C_p^{CPCM} the specific heat capacity of the CPCM, Σ represents the summation over all components in the composite, x_i, mass fraction of component i in the composite and $C_{p,i}$, the specific heat capacity of component i.

This equation enables us to systematically evaluate how the blending of different PCMs and matrix materials, such as MgO, influences the overall C_p of the composite. MgO was selected as the matrix material for all the CPCMs as it is currently the most frequently reported skeleton material and is performing quite well [11]. By applying this theory, the thermal behavior of CPCMs can be predicted with greater accuracy, facilitating PBLHS systems design which is finely tuned to the demands of various waste heat streams. The latent heat is obtained in a similar manner.

For the thermal conductivity Li and Ding recently conducted an extensive evaluation of various known empirical formulas for the prediction of the thermal conductivity of CPCMs [59]. They identified that of known relationships that of Ratcliffe performs best [60]. To this end, this was employed to predict the effective thermal conductivity values using the respective thermal conductivity of the PCM, depending on its melting point, and that of MgO, referenced from the literature [61]. In COMSOL software, the temperature-dependent thermal conductivity for each PCM was inputted as an interpolation function. It should be noted that the melting point of the PCM for each layer had at least one degree of difference from the other ones.

As mentioned, the properties of the CPCMs are defined as a function of their respective melting points. To accomplish this, a thorough literature investigation was conducted to identify PCMs in the temperature range examined in this work that are compatible with MgO. These are presented in Table 2.

In Fig. 2, a snapshot of the model is depicted. The tank exhibits three distinct layers, flanked by two free-flow regions representing the space between the flanges and the primary packed bed section. The depicted lengths of the PCM layers are representative; in actual simulations, these lengths are variable. It should be noted that the charging occurs with a direction opposite to discharging in order to maximize efficiency.

The effectiveness of the prediction model was contingent on the uniformity of the data sampling process. To achieve this uniformity, a significant number of diverse parameter combinations representing the entire spectrum of possible combinations were randomly selected. Among the various methods available for this purpose, Latin Hypercube Sampling (LHS), was identified as the most commonly utilized modern experimental design technique [62]. LHS is adept at uniformly sampling multiple parameter combinations, ensuring a robust dataset for the predictive model.

In this study, 832 datasets were generated using LHS. After eliminating datasets with potential errors and outliers, 620 were retained for training the machine learning model (Fig. 3). An initial selection included close to 10.000 individual cases; however, the R^2 values did not significantly differ from those derived from the smaller dataset ($<$3%). Each case was resolved to 2 decimal places. However, for many variables, this level of precision exceeds practical measurement capabilities, especially considering the limitations of measurement devices in TES systems such as temperature readings from thermocouples. Prior studies have used datasets encompassing over 20.000 cases, which may be excessive.

2.3. Machine learning model

Deep learning (DL) provides a robust tool for predicting heat storage and extraction in PBLHS. This is another advantage of the current study as opposed to the state-of-the-art where regression ML is employed. With its multi-layered neural networks, DL excels in representing hierarchical features and automatically learning them from raw data. This allows for
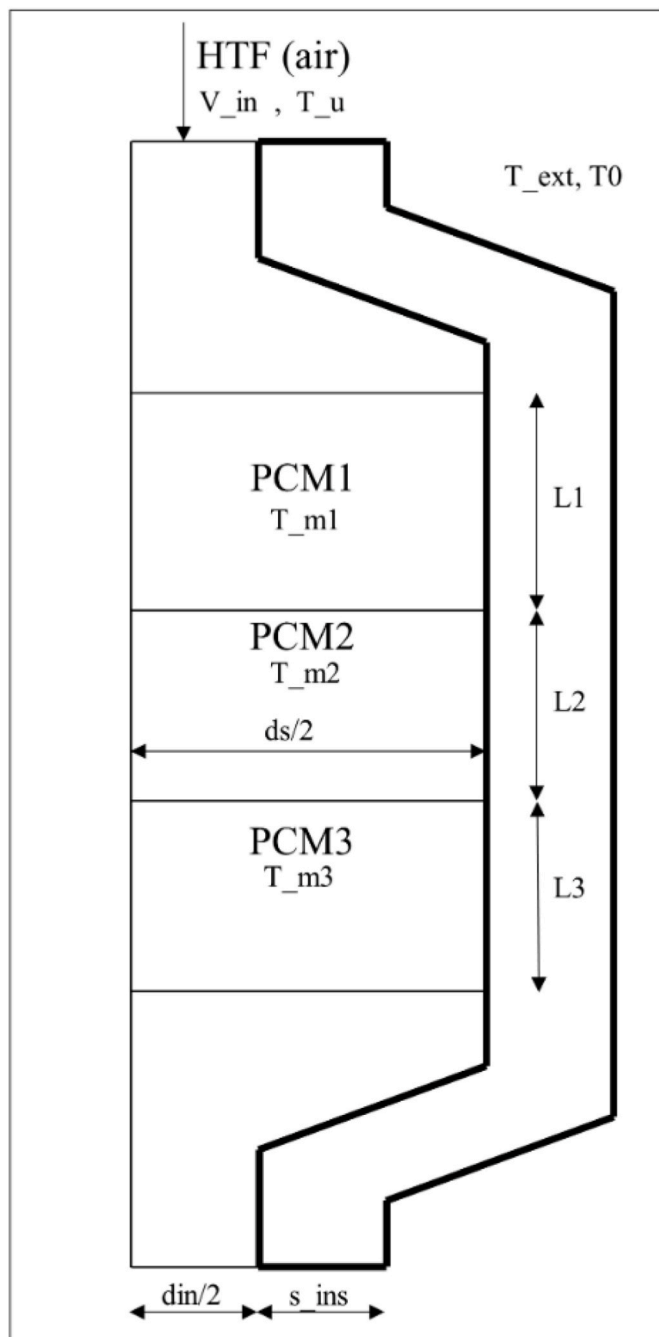

Fig. 2. Visualization of variables examined in the neural network.

higher data abstraction, yielding superior generalization to unseen data. Moreover, deep models facilitate end-to-end learning and transfer learning, where knowledge from one task can be more easily applied to another.

To characterize the PBLHS's behavior, a thorough investigation is conducted by solving the 2D-axisymmetric fluid dynamics and heat transfer equations for each data point in the generated dataset. This leads to determining the heat stored and extracted across different scenarios.

DL techniques are then employed. Two distinct neural networks are trained using the dataset. One network predicts the heat stored, while the other predicts the heat extracted by the system. These networks are trained to learn the intricate relationships between the input variables (Tables 1 and 2) and the corresponding heat storage/extraction values (Eqs. (17) and (18)). The model's input variables are categorized into
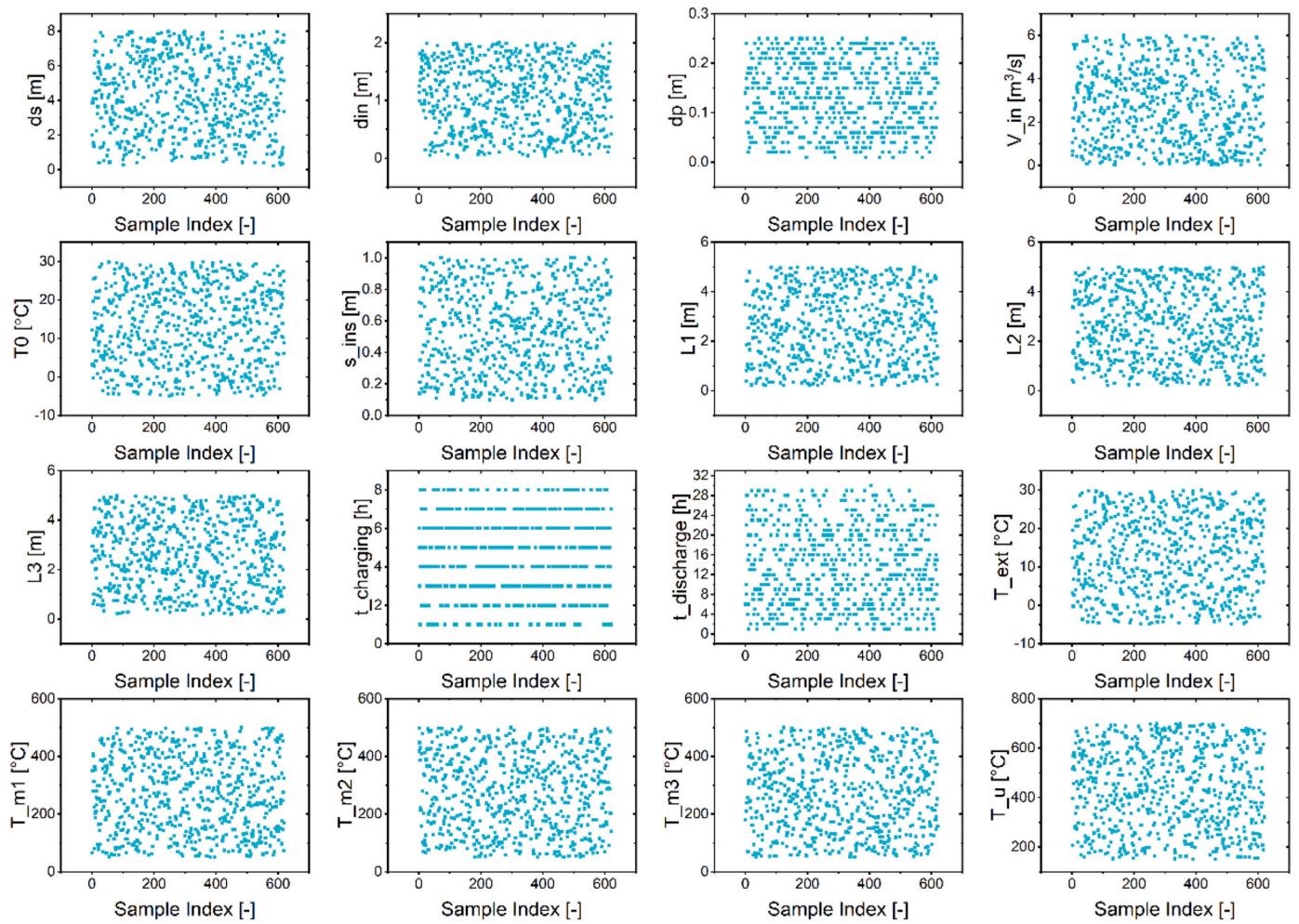
Fig. 3. Scatter plots of 620 points used for training a machine learning model, sampled via Latin Hypercube Sampling.
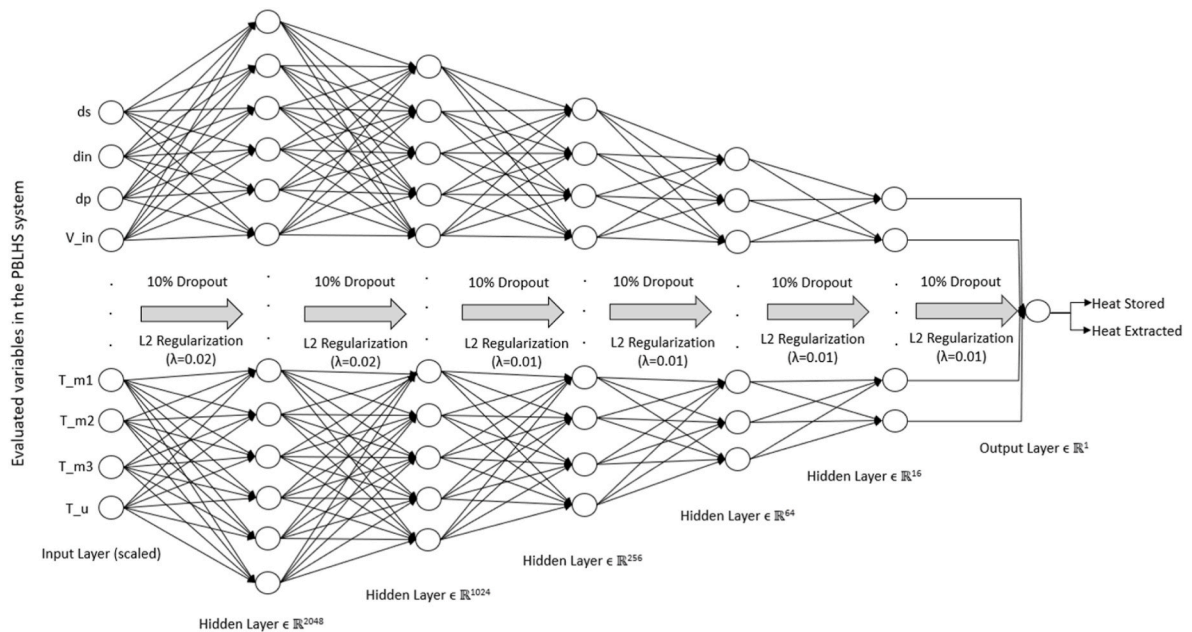

Fig. 4. The neural network used to evaluate the PBLHS, with inputs for system parameters, and outputs for heat stored and extracted, incorporating dropout and regularization techniques.

three groups: Design Variables, Time Variables, and Temperature Variables. Design Variables include storage tank diameter, inlet diameter, particle radius, inlet volumetric flow rate, insulation thickness, and lengths of three storage tanks. Time Variables encompass charging and discharge times, while Temperature Variables involve parameters like initial temperature, external temperature, melting points of phase change materials (CPCM), and upstream temperature.

Following data generation, the specific neural network architecture was designed. The complexity and nuances of the PBLHS guided the decision to choose a deep architecture with increasing layer sizes (Fig. 4). The primary objective centred on balancing model complexity with generalization capacity. Each layer and parameter was designed to address specific challenges in predictive modelling, such as overfitting and capturing intricate input-output relationships.

To optimize the predictive performance of the neural network architecture, preprocessing was imperative, including the standardization of input features using a StandardScaler. The standardized inputs are categorized into X_train_scaled and X_test_scaled. Due to the complexity of the PBLHS, with variables of varying scales it helps to place variables on a common scale as it enables the neural network to weigh each input more effectively.

The final neural network architecture begins with a dense layer of 2048 units using ReLU activation, transitioning through layers of 1024, 256, 64, and 16 units, with appropriate regularizations, including dropout layers and L2 penalty. ReLU activation was employed for nonlinear transformations. L2 regularization was used to control overfitting. The final layer, a single unit, outputs continuous values suitable for regression tasks. This comprehensive architecture is engineered for balance, regularization, and feature extraction, enabling robust generalization to unseen data.

The coefficient of determination (R2) is applied to evaluate the trained neural networks' accuracy. Furthermore, the Mean Absolute Percentage Error (MAPE) was also chosen as a metric for quantifying discrepancies. MAPE is calculated as:

$$MAPE = \frac{1}{n} \sum_{i=1}^{n} \left| \frac{Actual_i - Predicted_i}{Actual_i} \right| \cdot 100 \tag{28}$$

Where, n is the number of data points and $Actual_i$ and $Predicted_i$ represent the true and predicted values at the ith data point respectively.

Furthermore, the residuals, which are the differences between the predicted and actual values, are subjected to a Shapiro-Wilk test. This test checks whether the residuals follow a normal distribution, a crucial assumption in many statistical analyses.

2.4. Optimization protocol

PBLHS, presents multilevel challenges that depend on a large number of variables. Optimizing such a system requires traversing an expansive solution space to determine maximal configurations. Given these complexities, traditional optimization methods can be computationally demanding.

Metaheuristics transcend traditional heuristics by offering advanced, often stochastic, strategies for problem-solving. These algorithms have an innate capability to navigate broad solution spaces efficiently, thereby uncovering high-quality solutions. In this work, an array of metaheuristic optimization algorithms are employed, each chosen based on their unique strengths relevant the problem domain. Each of these algorithms was integrated with the neural network model described above. This combination capitalizes on the neural network's capability to estimate heat extraction values rapidly, thus offering the metaheuristics a swift approximation of system behaviour. This expedites the optimization process and ensures a thorough evaluation of each algorithm's adaptability and efficiency. These algorithms are:

2.4.1. Harmony Search

The Harmony Search (HS) algorithm is an innovative optimization methodology, conceptualized by Z.W. Geem and colleagues in the early 2000s [63]. This algorithm draws inspiration from the musical process of searching for a harmonious melody. Just as a composer experiments with combinations of notes to achieve an aesthetically pleasing harmony, the HS algorithm explores the solution space of an optimization problem to find the best possible solution. This approach has been successfully applied to various fields, such as groundwater modeling, structural design, energy dispatching, water network distribution, vehicular routing, and function optimization, among others. Its effectiveness is partly due to its ability to mimic the improvisation of musicians, translating this into the mathematical process of finding globally optimized solutions y_{i+1} based on the existing solution y_i can be expressed as:

$$y_{i+1} = y_i + H \times (2 \times \text{random\_number} - 1) \tag{29}$$

where, *random_number* is a randomly generated value within the range [0,1], and H represents the bandwidth, which determines the extent of local solution variations.

To enhance the variety of solutions and prevent convergence to local optima, a randomization factor is introduced:

$$R_{new} = R_{min} + (R_{max} - R_{min}) \times \text{random\_number} \tag{30}$$

where, R_{new} denotes the new randomized component, with R_{max} and R_{min} defining the upper and lower bounds, respectively. The likelihood of implementing a purely random search is:

$$P_{rand} = 1 - P_{accept} \tag{31}$$

where P_{rand} is the probability of selecting a completely random solution, and P_{accept} is the probability of accepting the new solution based on certain criteria within the algorithm. Consequently, the actual probability of applying pitch adjustment in the solution is quantified as:

$$P_{adjust} = P_{accept} \times R_{new} \tag{32}$$

Where P_{adjust} is the probability of adjusting the current solution to a new value, influenced by the degree of randomness R_{new}

The HS algorithm includes a mechanism to fine-tune solutions, analogous to adjusting musical pitch. Typically, adjustments to the pitch are made in a linear fashion, although the theoretical framework allows for nonlinear modifications. Through these components, the HS algorithm dynamically balances between explorative random searches and exploitative pitch adjustments to iteratively converge on the optimal solution.

2.4.2. Genetic algorithm (GA)

The Genetic Algorithm (GA) is a search heuristic that is inspired by Charles Darwin's theory of natural evolution. This algorithm reflects the process of natural selection where the fittest individuals are selected for reproduction in order to produce offspring of the next generation. The GA technique is routinely used to generate high-quality solutions to optimization and search problems by relying on bio-inspired operators such as mutation, crossover, and selection.

The fundamental concept of the GA is designed to simulate the survival of the fittest among individual solutions over consecutive generations. For each generation, a new set of approximations is created by the process of selecting individuals according to their level of fitness in the problem domain and breeding them together using operators borrowed from natural genetics. This process leads to the evolution of populations of individuals that are better suited to their environment than the individuals that they are made from, just as in natural adaptation.

A typical GA cycle includes the following steps, which can be represented in a pseudocode format.

1. Initialization - Generate an initial population of candidate solutions randomly.
2. Fitness Evaluation - Evaluate each candidate's fitness in the population.
3. Selection - Select candidates based on their fitness scores for reproduction.
4. Crossover - Breed new candidates through crossover (recombination) of parents.
5. Mutation - Mutate new candidates at random.
6. Replacement - Replace the current population with the new generation.

Mathematically, the GA can be modelled using the following expressions:

Let $P(t)$ represent the population at generation t, the process of creating a new generation $P(t+1)$ can be expressed as:

$$P(t+1) = \text{crossover}(\text{selection}(P(t))) \tag{33}$$

$$P(t+1) = \text{mutation}(P(t+1)) \tag{34}$$

where, *selectionP(t)* function chooses the fitter individuals from $P(t)$, *crossover* function breeds new individuals by combining aspects of the selected individuals, and *mutation* function introduces variations.

The fitness of each individual I in the population is evaluated using a fitness function f:

$$\text{fitness}(I) = f(I) \tag{35}$$

The selection process can be represented as:

$$\acute{I} = \text{select}(P(t)) \tag{36}$$

where $\acute{I}$ is the individual selected from the population $P(t)$.

The crossover and mutation operations introduce the genetic diversity and are defined as:

$$I_{\text{new}} = \text{crossover}(I_1, I_2) \tag{37}$$

$$I_{\text{mutated}} = \text{mutation}(I_{\text{new}}) \tag{38}$$

Where I_1 and I_2 are parent individuals, I_{new} is the offspring after crossover, and I_{mutated}.

is the offspring after mutation.

These equations and operators guide the GA towards the discovery of optimal or near-optimal solutions by exploring and exploiting the search space in a manner akin to biological evolution.

2.4.3. Ant Colony Optimization (ACO)

Ant Colony Optimization (ACO) is a probabilistic technique for solving computational problems which can be reduced to finding good paths through graphs. This algorithm is inspired by the behavior of ants in finding paths from their colony to food sources. The pioneering work by Dorigo in the early 2000s introduced this innovative approach, which has since been applied to various complex problems, from routing to scheduling and beyond [64].

In the ACO algorithm, a number of artificial ants build solutions to the optimization problem and improve them by mimicking the way real ants find the shortest paths to food. Each ant explores the search space and probabilistically selects the next state based on the pheromone trails and the heuristic information (e.g., the distance to the destination).

The pheromone value on path e from node i to node j for ant a, which reflects the learned desirability of choosing that path, can be expressed as follows:

$$\Delta\tau_{ij}^a = \frac{1}{L^a} \text{ if } a_{th} \text{ ant travels from edge i to g, otherwise } 0 \tag{39}$$

where L^a is the length of the tour constructed by ant a. The shorter the

tour, the larger the amount of pheromone deposited, inversely proportional to the tour length.

The residual pheromone on path e from node i to node j after all ants have completed their tours and before the new pheromone is laid down is given by:

$$\tau_{ij}^r = \sum_{a=1}^{m} \tau_{ij}^a \tag{40}$$

where m is the total number of ants. The updated pheromone trail, considering the evaporation rate, is then:

$$\tau_{ij}^{\text{new}} = (1-\rho)\cdot\tau_{ij} + \tau_{ij}^r \tag{41}$$

where ρ is the evaporation rate. If ρ is set to 1, all pheromone evaporates before new pheromone is added; if it is set to 0, there is no evaporation.

The Ant Colony Optimization algorithm utilizes a heuristic desirability η_{ij}, which is defined as the inverse of the distance $L_{i,j}$ between nodes i and j, to guide the search towards shorter paths:

$$\eta_{ij} = \frac{1}{L_{i,j}} \tag{42}$$

With this heuristic. the probability that ant a in node i chooses to move to node j is calculated by:

$$P_{ij}^a = \frac{(\tau_{ij})^\alpha \cdot (\eta_{ij})^\beta}{\sum (\tau_{ij}) \cdot (\eta_{ij})} \tag{43}$$

where α and β are parameters that control the influence of the pheromone trail and the heuristic information, respectively, and η_{ij} is the heuristic desirability of moving from node i to node j.

This probability equation integrates both the learned experience of the ants, represented by the pheromone trails, and the problem-specific heuristic.

The objective is to find the shortest path P, which is the sequence of nodes with the maximum product of pheromones and heuristic desirability, represented as:

$$P = \underset{P}{\text{argmax}} \left(\prod_{(i,j)\in P} (\tau_{ij} \cdot \eta_{ij}) \right) \tag{44}$$

where, the product inside the maximization is taken over all edges (i,j) that are part of the path P, and the argmax function selects the path that maximizes this product, fulfilling the goal of the optimization process.

These formulas highlight the essence of the ACO algorithm, where ants iteratively construct solutions and simulate the laying down of pheromones to guide subsequent ants, converging over time to the shortest or most optimal path.

2.4.4. Wind-Driven Optimization (WDO)

The Wind-Driven Optimization (WDO) algorithm is a nature-inspired metaheuristic optimization algorithm that simulates the motion of air particles in the atmosphere to solve optimization problems. Introduced by Bayraktar et al., in 2013, the WDO algorithm is recognized for its group-based iterative approach to global optimization, offering a balance of exploration and exploitation to efficiently converge towards global optima and avoiding premature convergence to local minima [65].

The WDO algorithm models the dynamics of air particle movement using the following update equations for velocity and position:

The new velocity of an air particle is computed by considering the current velocity, the gravitational force, the effect of air particle mass (rank), and the Coriolis force. The mathematical representation of the new velocity v_{new} is given by:

$$v_{new} = (1 - \alpha)v_{cur} - gv_{cur} + \left(\frac{RT}{i} - 1\right)\left(x_{opt} - x_{cur}\right) + c_{otherdim}\frac{cv_{cur}^{otherdim}}{i} \qquad (45)$$

where, v_{new} is the new velocity, v_{cur} is the current velocity, α is the friction coefficient, g is the gravitational acceleration, RT is a factor involving the universal gas constant and temperature, i represents the rank of air molecules, x_{opt} is the current optimal position, x_{cur} is the current position, $v_{cur}^{otherdim}$ is the velocity component of air particles in this dimension influenced by any other dimensions and c is the Coriolis force coefficient, expressed as:

$$c = -2\left[\Omega\sqrt{PR'}\right] \qquad (46)$$

Where c is the Coriolis force coefficient, Ω represents the rotational effect, and PR' is a modified term that includes the product of pressure and a modified gas constant. This term is used in the velocity update equation of the Wind-Driven Optimization algorithm.

The new position of the air particle is then updated based on its new velocity:

$$x_{new} = x_{cur} + v_{new}\Delta t \qquad (47)$$

This equation updates the current position x_{cur} by adding the product of the new velocity v_{new} and the time interval Δt, effectively simulating the displacement of the air particle within the search space.

The WDO algorithm utilizes these update rules iteratively, simulating the natural process of wind movements to distribute air particles throughout the search space, thereby searching for the optimal solution to the given problem. The algorithm's performance has proven effective in various fields, particularly in electrical engineering applications as demonstrated by its initial application.

3. Results and discussion

3.1. CFD model validation and independence testing

The CFD model employed in this work has already been validated by the COMSOL team using the data from the work of Nallusamy et al. with water as the HTF [66]. Furthermore, in a more recent work, Rabbi and Asif again validated the model using the same data, which found that despite minor differences in PCM properties and potential heat transfer variables, numerical results closely aligned with experimental data, with errors under 3%.

Nevertheless, to ensure the robustness of the proposed model, which uses air as the HTF, further validation was undertaken using two distinct studies: one at medium-high temperature and another at low. This

approach demonstrated the model's capacity to simulate the physics across the specified temperature range accurately.

The primary objective was to assess the disparity between the simulated temperature profiles and the corresponding experimental data. To achieve direct comparison, spline interpolation was utilized to enable a direct comparison despite differences in temporal resolution between experimental and simulation datasets.

For the first study chosen for validation, the setup features a cylindrical storage tank which was established by Bellan et al. [67]. The tank is made of carbon steel and houses 770 capsules, each with an average diameter of 0.0275 m and yielding a tank porosity of 0.345. The packed bed section is 0.254 m long, flanked by two 0.127 m free flow regions, and the inlet diameter measures 0.22 m. The external tank surface is shielded with a 0.1524 m thick insulation layer. During the charging process, the inlet temperature was maintained at 326 °C, with an initial temperature of 286 °C. Conversely, for the discharging process, the initial temperature was set at 326 °C, and the inlet temperature was reversed to 286 °C. The flowrate was consistently held at 110 m³/h throughout these operations. Given the uncertainty in experimental tests, the simulation results almost overlap with the experimental ones for this study (Fig. 5). The largest noted error is at 230min, which is 1.63%. The average experimental-to-simulation error is 0.46%.

The second validation study was based on experimental data by M.A. Izquierdo-Barrientos et al. Their setup utilized a well-insulated packed bed (glass-wool, 2 cm thickness) filled with GR50 spheres with a diameter of 1.64 mm [67]. The packed bed section had dimensions of 200 mm in both length and height. Air, channelled through a sieve at the bottom of the bed, was introduced at an inlet temperature of 65 °C with an initial bed temperature set at 15 °C. For the discharge phase, the temperature was 27 °C. The employed air mass flow rate was 450 l/min. A marginal deviation is noted during the charging phase, with simulations suggesting a minor lag near full charge.

Conversely, the discharging phase is well-represented in the simulations, with slight variations in the gradient of the phase change plateau. The most significant divergence is during the charging phase at the 0.64 h mark, with a temperature difference of 9.2 °C. Nevertheless, the average error is 4.47%, which demonstrates good agreement.

To ensure the model's accuracy, a sensitivity analysis was conducted to validate the impact of grid and timestep resolution on the results. The 2nd case, exhibiting the highest error, served as the benchmark for comparing experimental and simulation data. Timestep independence was examined at intervals of 0.05, 0.1-, and 0.5-min. Grid independence was evaluated by adjusting the mesh resolution using COMSOL's standard presets: coarse, coarse, normal, fine, and extrafine. Despite the computational load increasing substantially when transitioning from a
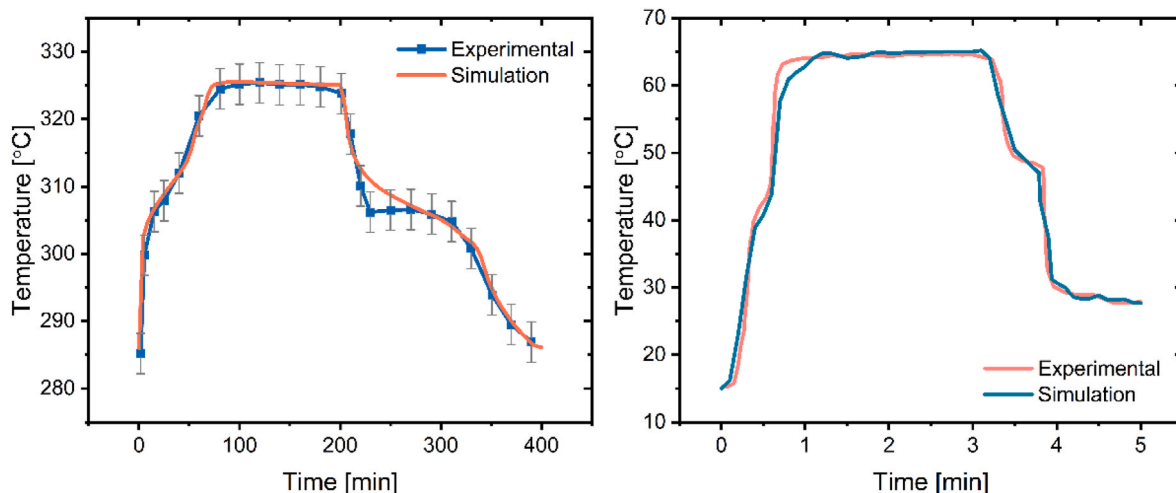
Fig. 5. Comparison of experimental with simulated data <u>Right</u>: First study [67] and <u>Left</u>: Second study [68].
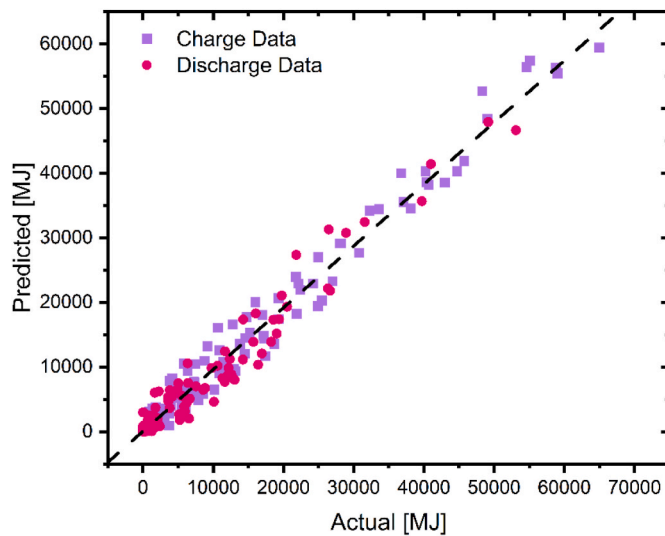
Fig. 6. Actual values predicted by the CFD model compared to values predicted by the deep neural network.

coarse to an extrafine grid, the error only reduced from 5.1% to 2.34%. Timestep variations showed a minimal impact, with a mere 0.38% error reduction observed in the 0.5-min interval.

3.2. Neural network evaluation

The scatter plots of both charge and discharge data sets provide comprehensive insights into the performance of the deep learning model (Fig. 6).

The model demonstrates a good capacity to predict outcomes across various energy scales for the charge data, which represents the storage process. A substantial portion of the data aligns closely with the 45-degree identity line, indicating the model's adeptness at capturing the fundamental dynamics of PBLHS. Nevertheless, some variations become evident, especially in higher value ranges. It's crucial to note that outliers, especially at the higher energy scales, suggest that room remains for further optimization. This can be potentially achieved through future continual refinement in model training.

The case is similar for the discharge data. Most points cluster around the identity line, suggesting effective predictions for most scenarios. However, the model still has instances, especially in the higher ranges, where it tends to either overpredict or underpredict.

The deep learning model's ability to predict across diverse scales is overall noteworthy. Its adaptability indicates a promising utility in guiding systems' design and performance assessment for both specific and general engineering applications in various scales and operational conditions.

The model's adaptability and performance across various scales are also underlined by the resulting R^2 values: 0.975 for charge and 0.974 for discharge. Such values indicate a significant alignment between the model's predictions and the actual data, capturing over 97% of the variability for both charging and discharging processes.

Further to the R^2, the neural network (NN) accuracy was assessed using the MAPE metric. This involved comparing the discrepancy between the calculated and predicted values for each case. The average MAPE for both charging and discharging cycles was ±9.17%. While this

level of accuracy is acceptable, it could potentially be enhanced by expanding the dataset, especially in regions characterized by outlier values.

In evaluating the residuals' distribution of the NN models, the Shapiro-Wilk test was administered to ascertain the normality of the data. The results of the NN Charge and NN Discharge residuals indicated p-values of 0.2738 and 0.1367, respectively (Table 3). Given that both p-values surpass the pre-determined significance threshold of 0.05, the test fails to reject the null hypothesis, implying that the residuals do not significantly deviate from a normal distribution. Effect sizes of 0.084 and 0.098 for the NN Charge and NN Discharge residuals, respectively, further underline this conclusion, suggesting that any deviation from normality is marginal. This adherence to the normal distribution among residuals is crucial, reinforcing the validity of the NN model and meeting fundamental assumptions prevalent in regression analyses.

Transitioning to the residuals of the model's predictions, similar observations are noted (Fig. 7). Examining the charge data's standardized residuals reveals an alignment with a standard normal distribution, predominantly centred around zero, indicating no consistent prediction bias. Yet, mid-range deviations in the −0.7 to −0.3 and 0.6 to 1 intervals suggest slight potential patterns not fully captured by the model. Similarly, a central clustering around zero emerges in the discharge data, emphasizing balanced predictions. A pronounced peak around the −0.2 region suggests a higher-than-expected frequency of residuals. Extreme residuals in both datasets, especially in distant regions like −2, 2, and beyond, align closely with the standard normal curve, which highlights the model's ability to minimize anomalous predictions.

3.3. Feature significance

A permutation importance technique was employed to understand the intricate dynamics of heat capture/extraction during the charging/discharging of the PBLHS. This is a method tailored for discerning feature significance within deep neural networks. At its core, this method shuffles a chosen feature's values while keeping the rest of the data intact, assessing how such alterations impact the neural network's performance. The resulting performance changes, quantified using the R^2 metric, quantify the prominence of that feature. The R^2 range is from 0 (indicating no model fit) to 1 (signifying perfect data fit). In this way, the variance in each respective variable can be gauged. This approach highlighted the critical features and illuminated the model's inner workings, enhancing its transparency.

In terms of the discharge phase, the heat captured, denoted as Q_{charge}, directly represents the energy stored in the PBLHS (Fig. 6). It is evident that the magnitude of heat captured during the charging phase, is a primary determinant of the heat that can be extracted during discharging.

The Discharge time, $t_{discharge}$, is the duration over which the system releases accumulated heat. Extended discharge phases ensure the extraction of a more significant portion of stored heat.

The storage tank's diameter stands out as the most important geometrical variable within the system, ranking third in importance. Visualizing the cascade system makes it evident that a larger diameter directly augments the volume of each layer, amplifying the total storage capacity. This amplification is because the tank's diameter impacts all three storage layers. A boost in total storage capacity offers greater potential for captured heat during the charging phase. This is realized through an enhanced thermal gradient, promoting more efficient heat transfer, a more extensive heat transfer area, and an overall larger

Table 3
Shapiro wilk test results.

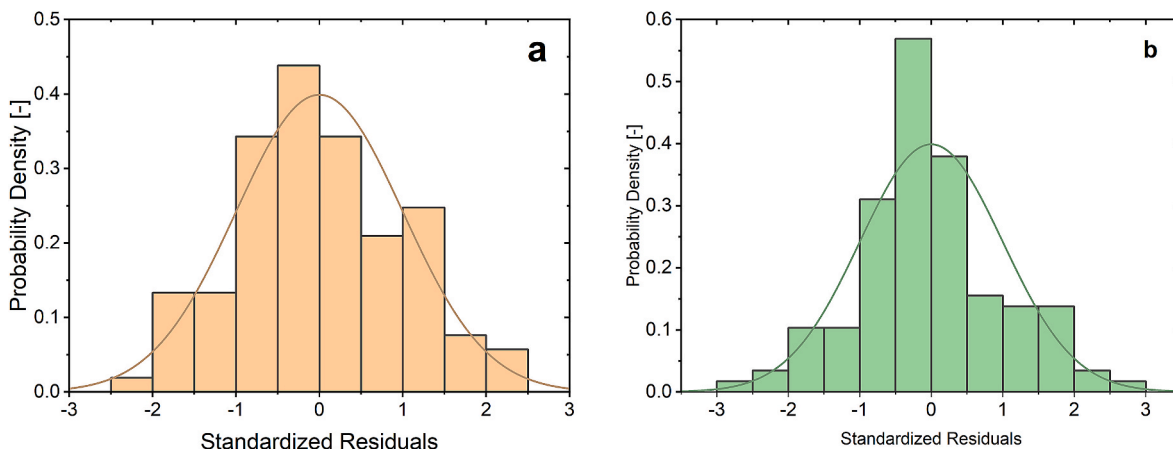| Dataset Name	Sample Size	Shapiro Wilk Test Statistic W	p-value	Significance level	Normality interpretation	Effect size
NN Charge Residuals	120	0.9848	0.2738	0.05	Not Rejected	0.084
NN Discharge Residuals	120	0.9825	0.1367	0.05	Not Rejected	0.098

Fig. 7. Histogram of Standardized Residuals for the charge data (a) and the discharge data (b).

storage volume. The system's cascade design, characterized by a sequence from higher to lower melting points from the inlet to the outlet, provides more context for the importance rankings. The zone with the highest melting point, likely due to its elevated threshold, might not achieve a full phase transition, particularly in non-optimal scenarios. This leads to potential underutilization of its latent heat storage capability. This is why the L2 and L3 are higher than L1.

Importance rankings also highlight the significance of storage tank lengths (notably L2 and L3) over specific melting points. This trend suggests a potential leaning towards sensible heat storage rather than latent heat in typical operational conditions. The reduced ranking of the melting point of CPCM1 supports this observation.

A point of interest is the limited importance ascribed to the inlet diameter. One might assume that the inlet diameter would significantly influence flow rate and heat exchange dynamics. However, results indicate potential underlying complexities in the system's behaviour. The volumetric flow rate becomes crucial given the specific flow conditions, perhaps overshadowing the direct effects of inlet diameter alterations.

Lastly, the role of insulation, gauged by its thickness, holds moderate importance within the analyzed operational conditions. Its significance might increase in scenarios characterized by extended idle states, which subject the system to larger heat losses. However, such idle periods were outside the scope of this analysis.

Looking at the charging phase, the Inlet Volumetric Flowrate stands out as the most prominent variable (Fig. 8). This is because its influence directly extends to the fluid's velocity, stemming from the momentum equation. A spike in this flow rate elevates fluid velocity, boosting the

convective heat transfer between the inlet fluid and the PCM capsules in the packed bed. This enhancement in heat transfer is significant, given that the convective term scales with fluid velocity.

The charging time introduces another layer of intricacy. It's not just about how high the temperature can get but how long the system can maintain it. A more extended charging process ensures that more heat gets accumulated. This continuous accumulation emphasizes that while the role of the inlet upstream (charging) temperature (T_u) might wane as the process advances and the temperature difference between the CPCM and the air narrows, the influence of charging time remains constant.

T_u is an important variable during the charging phase. Alongside the volumetric flowrate, it dictates the available heat for capture. When the capturing process starts, the temperature gradient between the inlet fluid and the PCMs is high, amplifying the heat transfer. However, as the charging advances, this difference starts to taper, causing a potential decline in the instantaneous heat transfer rate. This is a reasonable explanation as to why its significance is not as high as the flow rate or the charging time.

The diameter of the storage tank (d_s) determines the basic heat storage capacity of the system by defining the total storage volume. However, when its influence is compared to the flow rate, charging time or upstream temperature, it is evident why it would rank lower, as these variables directly affect the rate and efficiency of heat transfer. Conversely, merely increasing the storage tank diameter doesn't assure a proportional increase in heat capture. While a larger tank offers greater heat storage potential, its effectiveness depends on factors like the rate of heat transfer and the temperature gradient driving that transfer. Additionally, being a static parameter doesn't provide the same
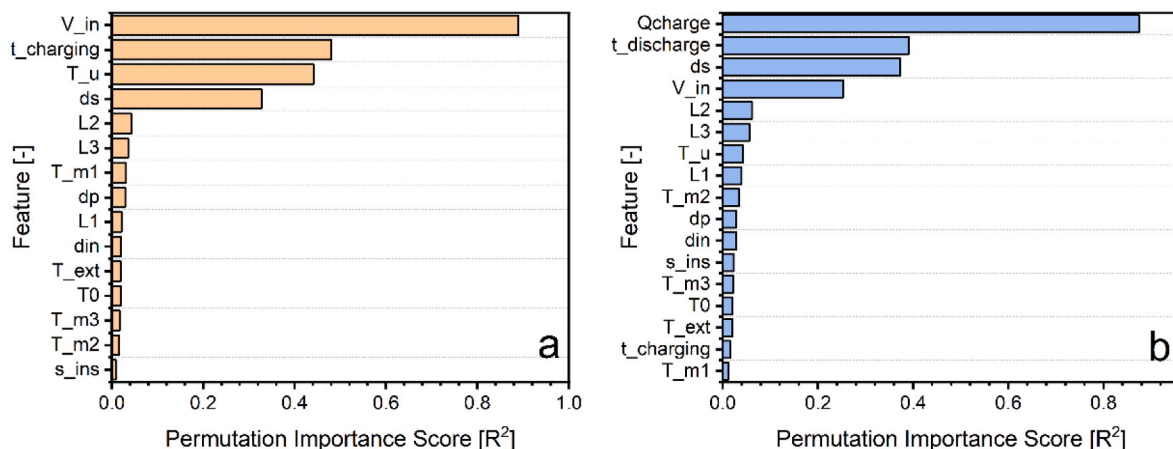

Fig. 8. Feature importance plot for the charge data (a) and the discharge data (b).

operational adaptability as the other dynamic parameters.

Along the same narrative and due to their lesser impact on the total storage capacity, as explained above, the storage tank lengths (L2 and L3) have even less influence.

A notable observation is the varied influence of the PCM melting points during charging and discharging. Tm1 is dominant in charging, while Tm2 is during discharging. This can be largely attributed to sequential melting and thermal stratification. During charging, the heat transfer fluid may first engage with CPCM1. Conversely, in discharging, the temperature gradient within the system is reversed and most probably favours CPCM2. This interplay of melting sequence and thermal gradient shapes the differential significance of these melting points.

Conversely, while the inlet diameter may seem pivotal to flow rate and heat exchange, its influence gets overshadowed by other dominant factors. Lastly, the Insulation Thickness confirms that the investigated scenarios are more inclined towards active heat exchange dynamics.

3.4. Optimization through metaheuristic algorithms

A series of diverse metaheuristic algorithms fit for this type of variable space is utilized to identify optimal designs that maximize heat capture and extraction. For each of these, the most pivotal task is achieving a fine balance between exploration and exploitation.

Exploration, in this context, is the effort to fully examine all the territories of the solution space, while exploitation is optimizing within already known areas. Exploitation often dictates an algorithm's efficiency, gravitating it towards the best solutions, whereas exploration ensures comprehensiveness, ensuring no potential solution is left untouched. As an initial study, three specific scenarios were examined for each algorithm: the first emphasizing a broad exploration, the second pivoting towards intensive exploitation, and the third seeking a harmonious blend of the two. An analysis of the preliminary optimization outcomes generated reveals several patterns and considerations.

A preliminary data scan shows that each algorithm uniquely manipulates and optimizes the design variables (Table 4). For instance, the spread in the ds values between different runs of the same algorithm (like GA1, GA2, and GA3) suggests that there's a broad exploration of potential solutions. However, certain consistent values within runs of a single algorithm hint at a deliberate exploitation of perceived optimal zones. In contrast, the ACO method leans more towards convergence. ACO's tendency to choose paths marked as promising is observable in the relatively clustered results across its runs, especially for parameters like ds.

Although some remarks can be made it is evident that the data doesn't exhibit any consistent pattern. For instance, with the Harmony Search (HS) series, while HS1's parameters, such as Tu at 357.45 °C, suggest exploration and HS2's value of 281.51 °C implies exploitation,

HS3 doesn't neatly fit into a median 'balanced' category as one might expect. Instead, it exhibits a unique mix of exploration and exploitation tendencies. GA is quite similar. While one might expect GA3 to fall between GA1 and GA2 consistently, the data suggests otherwise. Similar observations are made for the ACO and WDO series. Individual algorithm versions within these series sometimes defy a clear progression from exploration to exploitation.

On examining variability, the HS series, especially between HS1 and HS2, shows significant differences, underscoring HS's adaptability. The GA series, notably between GA1 and GA3, showcases its capacity for exploration and balance. The ACO series shows consistency. While WDO shows few anomalies, such as the remarkably high din value in WDO1. Such outliers might stem from the inherent stochastic nature of the algorithm.

Building on this observation, an intriguing aspect is illustrated through the data presented in Table 4, which reveals the model's strategic use of cascade features. This is particularly pronounced in cases such as WDO3 and HS3. Here, we observe that one layer, L1, is markedly shorter than L2 or L3. This disparity in layer lengths exemplifies the model's dynamic approach to design optimization: it not only explores various combinations to pinpoint the most efficient design but also intelligently discerns when a two-layer system, as opposed to a three-layer one, might suffice. Such discernment reflects a 'backward design' philosophy—understanding that at times, the exclusion of an additional layer could lead to a more optimal outcome. The model, therefore, not only proposes configurations but also critically evaluates the necessity of each component within the broader context of system efficiency.

Next up, the relationship between computational time and the objective of maximizing heat extraction is investigated where there is an inherent relationship between exploration and exploitation (Fig. 9).

GA1 and GA3, required longer computational times, but their corresponding heat extraction values varied notably. This suggests that while GA3 may have adopted a more balanced strategy between exploration and exploitation, GA1 leaned more towards exploration, as it consumed substantial time but didn't achieve the highest extraction values. GA2, however, had the lowest computational time and highest heat value, suggesting that an exploitation-rich search can be more fitting for how this algorithm tackles this problem.

On the other hand, ACO1 despite having a higher computational time than ACO3, did not have a higher extracted heat amount. This suggests that a balanced approach can be more efficient for these algorithms when looking at similar problems.

WDO1 and 3, although having the largest computational times also showcased the second and third-highest heat extraction values. On the other hand, WDO2 consumed less time but yielded the lowest extraction value, which perhaps means that an exploitation approach is the worst

Table 4
Neural network enhanced metaheuristics optimization results.

| Optimal Value	GA1	GA2	GA3	ACO1	ACO2	ACO3	WD01	WDO2	WD03	HS1	HS2	HS3
ds	2.06	2.97	1.99	2.53	2.93	1.4	2.9	1.14	2.83	2.51	1.09	2.21
din	0.43	0.55	0.95	0.41	0.22	0.76	9.67	0.54	0.75	0.31	0.51	0.99
dp	0.021	0.11	0.026	0.023	0.4	0.054	0.01	0.8	0.01	0.19	0.06	0.055
V_in	5.39	5.53	5.36	5.46	5.5	5.98	5.96	3.47	6	5.47	4.89	5.97
TO	34.76	−3.76	7.97	14.68	19.42	1.89	19.31	−1.86	−1.79	6.2	29.36	31.88
s_ins	0.38	0.16	0.93	0.92	0.03	0.23	0.01	0.34	0.01	0.17	0.81	0.18
L1	1.47	3.06	4.41	2.79	5.33	5.82	0.75	2.89	0.1	5.13	5.55	3.39
L2	5.18	2.84	3.46	3.06	5.32	5.66	1.13	4.44	4.66	2.42	5.11	5.63
L3	4.7	5.85	3.43	5.69	2.92	3.27	5.91	0.63	3.78	5.46	0.95	5.39
t_charge	8.11	9.72	8.82	7.88	9.56	9.48	10	6.87	10	9.29	9.74	9.79
t_discharge	19.72	10.7	3.52	14.48	17.2	19	4.72	19.82	10.97	19.28	19.37	18.57
T ext	14.65	−4.95	27.72	9.54	24.49	4.45	18.61	25.89	28.87	26.69	5.56	2.07
T_ml	351.43	89.04	445.13	206.69	219.99	323.9	459.74	472.64	497.02	485.25	367.29	483.09
T m2	441.32	449.94	422.89	417.89	447.01	202.79	413.04	472.32	496.81	461.81	447.99	483
T m3	413.92	381.87	392.48	394.01	446.99	285.23	105.41	236.77	162.23	461.81	447.99	470.02
T_u	294.82	276.26	372.73	394	313.31	285.24	363.17	273.65	150.3	357.45	281.51	364.56
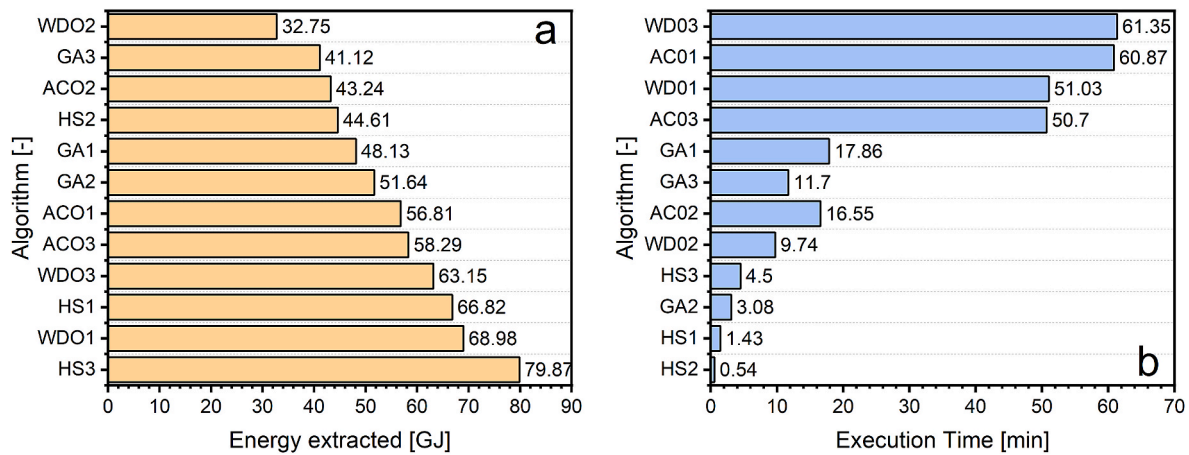
Fig. 9. Comparison of algorithms evaluated in terms of the execution time (a) and the objective function value (b).

for this type of algorithm in this specific design space.

HS algorithms were by far the best timewise. HS1, with a relatively short computational time of 85.96 s, and achieved an impressive heat extraction of 66.81 GJ. It's more balanced HS3 version showed the best value yet at 79 GJ with roughly only 3 times the computational demand.

HS algorithms emerge as clear frontrunners for optimizing this specific problem. An exhaustive grid search was executed to refine the HS algorithm's performance, focusing on determining the optimal hyperparameter configuration.

Key hyperparameters, including the number of harmonies, maximum iterations, harmony memory consideration rate, and pitch adjustment rate, were varied methodically. This systematic approach ensured a comprehensive exploration, top-tier optimization performance, and efficient use of computational resources.

The optimal hyperparameter configuration resulted in an objective function value of 95.9 GJ. This is impressive as its almost three times what is reported by WDO2, the worst-performing algorithm. It underscores the importance of methodical hyperparameter tuning in unveiling top-performing solutions in intricate engineering contexts like the one at hand.

3.5. A short case study

To highlight the proposed methodology's effectiveness, this section compares it with results from other studies (Table 5). The data used for this comparison has been extracted from various literature sources, reflecting different setups and temperature conditions. Overall, it can be seen that the model has a distinct edge in all 4 presented scenarios. It

Table 5

Comparative analysis of experimental and modelled results across different scenarios.

Reference	1 [69]	2 [67]	3 [31]	4 [70]
Experimental				
Charging Temperature (°C)	465	326	375	65
Flow Rate (m³/s)	0.0129	0.03056	0.00862	0.00750
Charging Duration (hours)	1.0	3.33	5.0	3.0
Discharge Temperature (°C)	325	286	50	30
Discharge Duration (hours)	1.33	3.33	3.33	2.0
Stored Energy [MJ]	7.44	3.96	26.41	2.54
Extracted Energy [MJ]	6.48	3.84	25.59	2.16
Charging efficiency [%]	91.5	72.3	76.4	50.5
Total efficiency [%]	79.7	70.1	74	42.9
Modelled				
Stored Energy [MJ]	7.66	5.01	31.11	4.22
Extracted Energy [MJ]	7.12	4.78	28.37	3.98
Charging efficiency [%]	93.6	92.8	90.3	84.4
Total efficiency (%)	87.0	88.5	82.4	79.6

should be noted that particularly cases 1 to 3 represent already experimentally optimized results.

In the comparative analysis, the optimized neural network (NN) model showcased improvements across all four metrics - stored energy, extracted energy, charging efficiency, and total efficiency - when compared with experimental data from various studies. The most notable enhancements were consistently observed in case 4, demonstrating the maximum enhancement across all metrics.

For stored energy, scenario 4 exhibited a remarkable 66.14% increase over its experimental counterpart. The second highest improvement in this category was observed in scenario 2, with a 26.52% increase. Similarly, in terms of extracted energy, scenario 4 again led with an impressive 84.26% enhancement, followed by scenario 2 showing a significant 23.96% increase.

The disparities in efficiencies were equally notable. In charging efficiency, scenario 4 showed a substantial improvement of 67.13%, while scenario 2 followed with a 28.35% increase. Total efficiency followed this pattern, with scenario 4 achieving an 85.55% enhancement over the experimental data, and scenario 2 witnessing an 26.25% improvement. The difference between experimental and modelled outcomes, particularly in efficiency metrics, sheds light on the potential improvements traditional PBLHS designs could realize through modern machine learning-enhanced approaches.

The optimized model's performance was closely examined also in terms of PCM operating temperatures during the four experimental scenarios. The general trend observed from the model's predictions was an increase in the total length of the tanks, aimed at achieving an improved aspect ratio beneficial for heat transfer. To optimize thermal gradient utilization, the model strategically incorporated additional PCMs with lower melting points.

For instance, in the first scenario, the model extended the packed bed height from 260 mm in the original study to 430 mm and introduced a second PCM with a melting point of 419 °C to exploit the maximum C_p, as illustrated in Fig. 1. This approach leverages the predominant role of sensible heat over latent heat in the energy storage process, considering the significant proportion of latent heat lost due to the encapsulation process. However, this selection, primarily based on thermophysical benefits rather than cost-effectiveness, resulted in a PCM composition that, while having a higher C_p, also entailed increased costs due to a greater lithium content. Subsequently, the model added a layer of KNO_3 with a melting point of 334 °C, above the initial environmental temperature, to leverage additional latent heat content.

In the second scenario, the model implemented a seemingly counterintuitive approach by increasing the length and reducing the diameter of the tank, then adding three PCMs with melting points of 310 °C, 303 °C, and 292 °C. This configuration was designed to maximize energy density and thermal gradient capture, despite appearing illogical from a

conventional design perspective.

The third scenario followed a similar logic, with the model extending the tank length and incorporating three PCMs with melting points of 283 °C, 187 °C, and 53 °C, aiming to further exploit the thermal gradient.

The final scenario saw the model doubling the tank length and integrating two PCMs at 50 °C and 52 °C. This case highlighted some limitations, as the materials with melting points below these temperatures were not inputted in the model, suggesting that even lower melting points could potentially yield higher efficiencies.

It is important to note that all proposed scenarios were validated using CFD simulations, with the heat extracted values being within 5.6% of the model's predictions. However, the model often failed to achieve a melting fraction of unity during the charging phase, which subsequently affected the discharging phase. This underlines the need for further modeling to seek a better balance between melting fraction and thermal inertia capture during discharging.

These promising findings across the four key TES performance variables highlight the significant potential of applying deep learning techniques to optimize traditional PBLHS designs. The consistent outperformance in all scenarios underscores the model's capability in handling a wide range of operating conditions effectively.

3.6. Charging/discharging Efficiency Trends

The significance of assessing the model's performance across a range of energy data cannot be understated. It's essential as it confirms the model's consistency in different operational scenarios. Considering the variability in waste heat streams' temperature, flow rate, and duration for both charging and discharging phases, a direct analysis can be challenging. To address this, the total energy value of the stream using equation (16) and setting T_{oulet} as $T0$ (ambient temperature), with the properties of air referenced from equations (25) and (26) for density and specific heat capacity, respectively. By generating over 100 data points and clustering them into energy intervals of 25 GJ, and ensuring a minimum of 6 values per bracket with weighted averages, the complexity of the data is managed correctly.

In analyzing these clusters, discharge efficiency is consistently higher than charging efficiency (Fig. 10). This is in line with the expectation that the model is optimized to maximize heat extraction, a process that often sees higher efficiency in discharging than in charging due to the inherent difficulty in finding equilibrium in these systems.
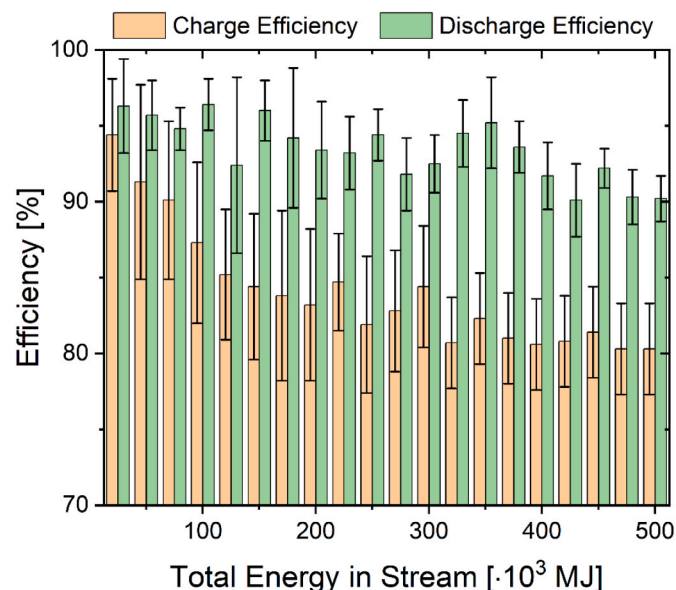

Fig. 10. Efficiency comparison for charged and discharged energy.

A correlation analysis between the PBLHS's efficiency and operational parameters reveals insightful trends. The correlation coefficients indicate a moderate negative correlation between the flow rate (V_in) and efficiency, with values of −0.341 for charging and −0.218 for discharging. This suggests that as the flow rate increases, the system's ability to charge efficiently decreases more significantly than its ability to discharge. The higher impact on charging can be attributed to the model's prioritization of discharge efficiency, where the design adaptations to minimize the effects of flow rate are less aggressive and secondarily due to increased thermal inertia that doesn't allow the medium to equilibrate with the heat source or sink quickly.

For the inlet temperature (Tu), the positive correlation coefficients are 0.133 for charging and 0.08 for discharging, indicating a less pronounced effect. The inlet temperature has a direct influence on the thermal gradient, which is more critical during the charging phase, as it drives the heat transfer into the storage medium. During discharging, the effect is secondary as the system is primarily concerned with extracting the stored heat.

The duration of the heat stream ($t\_charging$), which was taken to be equal to t_*discharging*, shows the strongest negative correlation with the system's efficiency, with coefficients of −0.548 for charging and −0.363 for discharging. This implies that extended durations are particularly detrimental to charging efficiency, likely due to accumulating losses over time. In the charging phase, the temperature rise is initially steep, which then tapers off, leading to a compounding effect on losses. Conversely, during discharging, the temperature rapidly decreases towards ambient levels, reducing the heat loss over time and resulting in a less strong correlation.

These coefficients reveal that the model's performance in terms of charge efficiency is more sensitive to operational parameters compared to discharge efficiency. The effects are especially more pronounced during charging because the model is less optimized to mitigate these influences. Specifically, the inlet temperature of the waste heat stream greatly affects the charging phase due to its significant role in establishing the necessary thermal gradient for heat transfer. In contrast, its effect during discharging is less impactful. The correlation analysis, coupled with the feature importance study, demonstrates that the design of the PBLHS is adept at handling variations during discharging, but there remains room for striking a balance in improvement during the charging phase to enhance overall efficiency.

4. Conclusions

Addressing the urgent need for efficient WHR in industries with high carbon emissions, this study introduces an innovative approach in TES. An novel approach for advanced design and optimization of PBLHS is presented. This leverages DL coupled with metaheuristics. The key takeaways are.

1. **Model Performance and Validity:** The developed deep learning model's adaptability across various scales was highlighted by the resulting R^2 values of 0.975 for charge and 0.974 for discharge, capturing over 97% of the variability for both processes. This was accompanied by a reasonable MAPE of <9.14%.
2. **Feature Significance:** A permutation importance technique was employed to discern feature significance within the deep neural networks. For the discharge phase, the heat captured was a significant feature, as it directly represents the dynamics of heat capture/extraction during the charging/discharging processes. For the charging phase, the inlet volumetric flowrate was noticeably important. This is because it influences the fluid's velocity, enhancing the convective heat transfer between the air and the PCM capsules.
3. **Optimization through Metaheuristic Algorithms:** An array of algorithms was employed to identify optimal designs that maximize heat capture and extraction. The HS algorithm emerged as the most

effective. Its performance was further refined through an exhaustive grid search. The optimal hyperparameter configuration achieved an objective function value of 95.9 MJ, almost three times higher than that reported by the WDO, the least effective algorithm. This underscores the importance of methodical hyperparameter tuning in intricate engineering contexts.

4. **Comparative Analysis:** The model is also compared with four experimental scenarios. In terms of energy storage and efficiency, the model consistently surpassed the experimental benchmarks. This was particularly noted in terms of total efficiency.

5. **Efficiency Trends:** A comprehensive analysis indicates a higher discharge efficiency over charge efficiency, a deliberate result of the model's optimization for heat extraction. Flow rate inversely affects charging efficiency more than discharging. Heat stream durations negatively impact efficiency, while inlet temperature has a more nuanced effect on the system's performance. Results are in alignment with feature importance study.

Conclusively, this research presents, for the first time, a novel approach that couples DL with metaheuristics to optimize PBLHS. This innovative method yields rapid designs that significantly advance the state of the art in TES. It is anticipated that this approach can be extended to other TES configurations in the future. Looking ahead, it is crucial for the model to incorporate cost considerations to facilitate more pragmatic decisions in the selection of PCMs or structural materials. Additionally, further refinement is essential, especially for scenarios involving higher magnitudes of energy, particularly in the context of heat storage—a distinct challenge compared to heat extraction, where the model currently demonstrates exceptional proficiency.

CRediT authorship contribution statement

Argyrios Anagnostopoulos: Writing – review & editing, Writing – original draft, Visualization, Validation, Supervision, Project administration, Methodology, Investigation, Funding acquisition, Formal analysis, Data curation, Conceptualization. **Theofilos Xenitopoulos:** Writing – review & editing, Writing – original draft, Visualization, Validation, Methodology, Investigation, Formal analysis. **Yulong Ding:** Software, Resources. **Panos Seferlis:** Writing – review & editing, Resources, Project administration, Funding acquisition.

Declaration of competing interest

The authors declare that they have no known competing financial interests or personal relationships that could have appeared to influence the work reported in this paper.

Data availability

Data will be made available on request.

Acknowledgements

References

[1] Ellabban O, Abu-Rub H, Blaabjerg F. Renewable energy resources: current status, future prospects and their enabling technology. Renew Sustain Energy Rev 2014; 39. https://doi.org/10.1016/j.rser.2014.07.113.

[2] European Commission. 2030 energy strategy, europa. 2016.

[3] IEA, Global Energy Review: CO2 Emissions in 2020. Glob. Energy Rev. 2021.

[4] Malinauskaite J, Jouhara H, Ahmad L, Milani M, Montorsi L, Venturelli M. Energy efficiency in industry: EU and national policies in Italy and the UK. Energy 2019; 172. https://doi.org/10.1016/j.energy.2019.01.130.

[5] Agathokleous R, Bianchi G, Panayiotou G, Aresti L, Argyrou MC, Georgiou GS, Tassou SA, Jouhara H, Kalogirou SA, Florides GA, Christodoulides P. Waste Heat Recovery in the EU industry and proposed new technologies. Energy Proc 2019; 161:489–96. https://doi.org/10.1016/j.egypro.2019.02.064.

[6] Jouhara H, Khordehgah N, Almahmoud S, Delpech B, Chauhan A, Tassou SA. Waste heat recovery technologies and applications. Therm Sci Eng Prog 2018;6: 268–89. https://doi.org/10.1016/j.tsep.2018.04.017.

[7] Miró L, Gasia J, Cabeza LF. Thermal energy storage (TES) for industrial waste heat (IWH) recovery: a review. Appl Energy 2016;179. https://doi.org/10.1016/j.apenergy.2016.06.147.

[8] Fernández AI, Barreneche C, Miró L, Brückner S, Cabeza LF, Fernández AI, Barreneche C, Miró L, Cabeza LF, Brückner S. Waste heat recovery using thermal energy storage. In: Adv. Therm. Energy storage syst.; 2021. https://doi.org/10.1016/b978-0-12-819885-8.00022-x.

[9] Palacios A, Barreneche C, Navarro ME, Ding Y. Thermal energy storage technologies for concentrated solar power – a review from a materials perspective. Renew Energy 2019. https://doi.org/10.1016/j.renene.2019.10.127.

[10] Jouhara H, Żabnieńska-Góra A, Khordehgah N, Ahmad D, Lipinski T. Latent thermal energy storage technologies and applications: a review. Int. J. Thermofluids 2020;5–6. https://doi.org/10.1016/j.ijft.2020.100039.

[11] Jiang F, Zhang L, She X, Li C, Cang D, Liu X, Xuan Y, Ding Y. Skeleton materials for shape-stabilization of high temperature salts based phase change materials: a critical review. Renew Sustain Energy Rev 2020;119:109539. https://doi.org/10.1016/j.rser.2019.109539.

[12] Anagnostopoulos A, Navarro ME, Stefanidou M, Ding Y, Gaidajis G. Red mud-molten salt composites for medium-high temperature thermal energy storage and waste heat recovery applications. J Hazard Mater 2021;413. https://doi.org/10.1016/j.jhazmat.2021.125407.

[13] Anagnostopoulos A, Navarro M, Ahmad A, Ding Y, Gaidajis G. Valorization of phosphogypsum as a thermal energy storage material for low temperature applications. J Clean Prod 2022;342:130839. https://doi.org/10.1016/J.JCLEPRO.2022.130839.

[14] Abdelsalam MY, Teamah HM, Lightstone MF, Cotton JS. Hybrid thermal energy storage with phase change materials for solar domestic hot water applications: direct versus indirect heat exchange systems. Renew Energy 2020;147. https://doi.org/10.1016/j.renene.2019.08.121.

[15] Felix Regin A, Solanki SC, Saini JS. An analysis of a packed bed latent heat thermal energy storage system using PCM capsules: numerical investigation. Renew Energy 2009;34:1765–73. https://doi.org/10.1016/J.RENENE.2008.12.012.

[16] Gautam A, Saini RP. A review on technical, applications and economic aspect of packed bed solar thermal energy storage system. J Energy Storage 2020;27: 101046. https://doi.org/10.1016/J.EST.2019.101046.

[17] Medrano M, Gil A, Martorell I, Potau X, Cabeza LF. State of the art on high-temperature thermal energy storage for power generation. Part 2—case studies. Renew Sustain Energy Rev 2010;14:56–72. https://doi.org/10.1016/J.RSER.2009.07.036.

[18] He X, Qiu J, Wang W, Hou Y, Ayyub M, Shuai Y. A review on numerical simulation, optimization design and applications of packed-bed latent thermal energy storage system with spherical capsules. J Energy Storage 2022;51:104555. https://doi.org/10.1016/J.EST.2022.104555.

[19] Ananthanarayanan V, Sahai Y, Mobley CE, Rapp RA. Modeling of fixed bed heat storage units utilizing phase change materials. Metall Trans B 1987;18:339–46. https://doi.org/10.1007/BF02656152/METRICS.

[20] Beasley DE, Ramanarayanan C, Torab H. Thermal response of a packed bed of spheres containing a phase-change material. Int J Energy Res 1989;13:253–65. https://doi.org/10.1002/ER.4440130302.

[21] Yagi J, Akiyama T. Storage of thermal energy for effective use of waste heat from industries. J Mater Process Technol 1995;48:793–804. https://doi.org/10.1016/0924-0136(94)01723-E.

[22] Liu HB, Zhao CY. Effect of radial porosity oscillation on the thermal performance of packed bed latent heat storage. Engineering 2021;7. https://doi.org/10.1016/j.eng.2020.05.020.

[23] Grabo M, Acar E, Kenig EY. Modeling and improvement of a packed bed latent heat storage filled with non-spherical encapsulated PCM-Elements. Renew Energy 2021; 173. https://doi.org/10.1016/j.renene.2021.04.022.

[24] Wang W, He X, Hou Y, Qiu J, Han D, Shuai Y. Thermal performance analysis of packed-bed thermal energy storage with radial gradient arrangement for phase change materials. Renew Energy 2021;173. https://doi.org/10.1016/j.renene.2021.04.032.

[25] Dong Y, Zhang X, Wang F, Zhang G, Shi X, Shuai Y. Numerical study on the thermal performance analysis of packed-bed latent heat thermal storage system with biomimetic vein hierarchical structure. Int J Green Energy 2022;19. https://doi.org/10.1080/15435075.2021.1952208.

[26] Nekoonam S, Ghasempour R. Modeling and optimization of a thermal energy storage unit with cascaded PCM capsules in connection to a solar collector. Sustain Energy Technol Assessments 2022;52. https://doi.org/10.1016/j.seta.2022.102197.

[27] Elsihy ElsS, Xu C, Du X. Cyclic performance of cascaded latent heat thermocline energy storage systems for high-temperature applications. Energy 2022;239. https://doi.org/10.1016/j.energy.2021.122229.

[28] Manente G, Ding Y, Sciacovelli A. A structured procedure for the selection of thermal energy storage options for utilization and conversion of industrial waste heat. J Energy Storage 2022;51. https://doi.org/10.1016/j.est.2022.104411.

[29] Wu X, Tang Z. Heat transfer and storage characteristics of a hexagonal close structured packed-bed thermal storage system with molten salt phase change materials. J Energy Storage 2023;65:107356. https://doi.org/10.1016/J.EST.2023.107356.

[30] Alptekin E, Ezan MA. A systematic assessment on a solar collector integrated packed-bed single/multi-layered latent heat thermal energy storage system. J Energy Storage 2021;37. https://doi.org/10.1016/j.est.2021.102410.

[31] He X, Qiu J, Wang W, Hou Y, Ayyub M, Shuai Y. Optimization design and performance investigation on the cascaded packed-bed thermal energy storage system with spherical capsules. Appl Therm Eng 2023;225. https://doi.org/10.1016/j.applthermaleng.2023.120241.

[32] Mao Q, Cao W. Effect of variable capsule size on energy storage performances in a high-temperature three-layered packed bed system. Energy 2023;273. https://doi.org/10.1016/j.energy.2023.127166.

[33] Mohammadnejad F, Hossainpour S. A CFD modeling and investigation of a packed bed of high temperature phase change materials (PCMs) with different layer configurations. J Energy Storage 2020;28. https://doi.org/10.1016/j.est.2020.101209.

[34] Zhang Z, Liang M, Cong Y. Analysis of thermodynamic performance of cascaded latent heat storage using variable diameter capsules. J Energy Storage 2022;55. https://doi.org/10.1016/j.est.2022.105595.

[35] Aziz NA, Amin NAM, Majid MSA, Bruno F, Belusko M. Optimising a packed bed phase change material of spheres using effectiveness-number of transfer unit method. J Energy Storage 2022;49. https://doi.org/10.1016/j.est.2022.104019.

[36] Gu GH, Noh J, Kim I, Jung Y. Machine learning for renewable energy materials. J Mater Chem A 2019. https://doi.org/10.1039/c9ta02356a.

[37] He Z, Guo W, Zhang P. Performance prediction, optimal design and operational control of thermal energy storage using artificial intelligence methods. Renew Sustain Energy Rev 2022;156. https://doi.org/10.1016/j.rser.2021.111977.

[38] Vakili M, Salehi SA. A review of recent developments in the application of machine learning in solar thermal collector modelling. Environ Sci Pollut Res 2023;30. https://doi.org/10.1007/s11356-022-24044-y.

[39] Kang X, Wang X, An J, Yan D. A novel approach of day-ahead cooling load prediction and optimal control for ice-based thermal energy storage (TES) system in commercial buildings. Energy Build 2022;275. https://doi.org/10.1016/j.enbuild.2022.112478.

[40] Ojih J, Onyekpe U, Rodriguez A, Hu J, Peng C, Hu M. Machine learning accelerated discovery of promising thermal energy storage materials with high heat capacity. ACS Appl Mater Interfaces 2022;14. https://doi.org/10.1021/acsami.2c11350.

[41] Cheng L, Zang H, Wei Z, Zhang F, Sun G. Evaluation of opaque deep-learning solar power forecast models towards power-grid applications. Renew Energy 2022;198. https://doi.org/10.1016/j.renene.2022.08.054.

[42] Li X, Yao R. A machine-learning-based approach to predict residential annual space heating and cooling loads considering occupant behaviour. Energy 2020;212. https://doi.org/10.1016/j.energy.2020.118676.

[43] Ermis K, Erek A, Dincer I. Heat transfer analysis of phase change process in a finned-tube thermal energy storage system using artificial neural network. Int J Heat Mass Tran 2007;50. https://doi.org/10.1016/j.ijheatmasstransfer.2006.12.017.

[44] Hofmann R, Halmschlager V, Koller M, Scharinger-Urschitz G, Birkelbach F, Walter H. Comparison of a physical and a data-driven model of a Packed Bed Regenerator for industrial applications. J Energy Storage 2019;23. https://doi.org/10.1016/j.est.2019.04.015.

[45] Li Z, Lv ST. Performance analysis and optimization of packed-bed TES systems based on ensemble learning method. Energy Rep 2022;8. https://doi.org/10.1016/j.egyr.2022.06.028.

[46] Mao Q, Zhang Y. Thermal energy storage performance of a three-PCM cascade tank in a high-temperature packed bed system. Renew Energy 2020;152. https://doi.org/10.1016/j.renene.2020.01.051.

[47] Bergman TL, Lavine AS, Incropera FP, DeWitt DP. Fundamentals of heat and mass transfer, 2011. USA John Wiley Sons; 2015. . ISBN. 13.

[48] Agalit H, Zari N, Maalmi M, Maaroufi M. Numerical investigations of high temperature packed bed TES systems used in hybrid solar tower power plants. Sol Energy 2015;122. https://doi.org/10.1016/j.solener.2015.09.032.

[49] Wang J, Lai M, Han H, Ding Z, Liu S, Zeng D. Thermodynamic modeling and experimental verification of eutectic point in the LiNO3-KNO3-Ca(NO3)2 ternary system. J Therm Anal Calorim 2015;119. https://doi.org/10.1007/s10973-014-4218-0.

[50] Xu F, Wang J, Zhu X, Liu X. Thermodynamic modeling and experimental verification of a NaNO3-KNO3-LiNO3-Ca(NO3)2 system for solar thermal energy storage. New J Chem 2017;41. https://doi.org/10.1039/c7nj02051a.

[51] Takahashi Y, Sakamoto R, Kamimoto M. Heat capacities and latent heats of LiNO3, NaNO3, and KNO3. Int J Thermophys 1988;9. https://doi.org/10.1007/BF01133275.

[52] Nomura S. Thermal properties of NaNO2. J. Phys. Soc. Japan 1961;16. https://doi.org/10.1143/JPSJ.16.1352.

[53] Ohkubo T, Ohnishi R, Sarou-Kanian V, Bessada C, Iwadate Y. Molecular dynamics simulations of the thermal and transport properties of molten NaNO2–NaNO3 systems. Electrochemistry 2018;86. https://doi.org/10.5796/electrochemistry.17-00094.

[54] Anagnostopoulos A, Alexiadis A, Ding Y. Molecular dynamics simulation of solar salt (NaNO3-KNO3) mixtures. Sol Energy Mater Sol Cells 2019;200:109897. https://doi.org/10.1016/j.solmat.2019.04.019.

[55] Anagnostopoulos A, Palacios A, Navarrete N, Navarro ME, Hernandez L, Ding Y. Effect of temperature on the internal structure of solar salt-SiO2. In: AIP conf. Proc.; 2019, 200003. https://doi.org/10.1063/1.5117718.

[56] Bradshaw RW. Effect of composition on the density of multi-component molten nitrate salts. Mater Chem 2009.

[57] Janz GJ, Neuenschwander E, Kelly FJ. High-temperature heat content and related properties for Li2CO3, Na2CO3, K2CO3, and the ternary eutectic mixture. Trans Faraday Soc 1963;59:841–5. https://doi.org/10.1039/TF9635900841.

[58] Janz GJ, Lorenz MR. Solid-liquid phase equilibria for mixtures of lithium, sodium, and potassium carbonates. J Chem Eng Data 1961;6. https://doi.org/10.1021/je00103a001.

[59] Li C, Li Q, Ding Y. Investigation on the effective thermal conductivity of carbonate salt based composite phase change materials for medium and high temperature thermal energy storage. Energy 2019;176. https://doi.org/10.1016/j.energy.2019.04.029.

[60] Ratcliffe EH. Estimation of the effective thermal conductivities of two-phase media. J Appl Chem 2007;18. https://doi.org/10.1002/jctb.5010180106.

[61] Slifka AJ, Filla BJ, Phelps JM. Thermal conductivity of magnesium oxide from Absolute, steady-state measurements. J. Res. Natl. Inst. Stand. Technol. 1998;103. https://doi.org/10.6028/jres.103.021.

[62] McKay MD, Beckman RJ, Conover WJ. A comparison of three methods for selecting values of input variables in the analysis of output from a computer code. Technometrics 2000;42. https://doi.org/10.1080/00401706.2000.10485979.

[63] Geem ZW, Kim JH, Loganathan G V. A New Heuristic Optimization Algorithm: Harmony Search. Simulation 2001;76. https://doi.org/10.1177/003754970107600201.

[64] Dorigo M, Birattari M, Stützle T. Ant colony optimization artificial ants as a computational intelligence technique, 1. IEEE Comput Intell Mag; 2006. https://doi.org/10.1109/CI-M.2006.248054.

[65] Bayraktar Z, Komurcu M, Bossard JA, Werner DH. The wind driven optimization technique and its application in electromagnetics. IEEE Trans Antennas Propag 2013;61. https://doi.org/10.1109/TAP.2013.2238654.

[66] Nallusamy N, Sampath S, Velraj R. Study on performance of a packed bed latent heat thermal energy storage unit integrated with solar water heating system. J Zhejiang Univ - Sci 2006;7. https://doi.org/10.1631/jzus.2006.A1422.

[67] Bellan S, Alam TE, González-Aguilar J, Romero M, Rahman MM, Goswami DY, Stefanakos EK. Numerical and experimental studies on heat transfer characteristics of thermal energy storage system packed with molten salt PCM capsules. Appl Therm Eng 2015;90. https://doi.org/10.1016/j.applthermaleng.2015.07.056.

[68] Loem S, Deethayat T, Asanakham A, Kiatsiriroat T. Thermal characteristics on melting/solidification of low temperature PCM balls packed bed with air charging/discharging. Case Stud Therm Eng 2019;14. https://doi.org/10.1016/j.csite.2019.100431.

[69] Li MJ, Jin B, Ma Z, Yuan F. Experimental and numerical study on the performance of a new high-temperature packed-bed thermal energy storage system with macroencapsulation of molten salt phase change material. Appl Energy 2018;221. https://doi.org/10.1016/j.apenergy.2018.03.156.

[70] Izquierdo-Barrientos MA, Sobrino C, Almendros-Ibáñez JA. Thermal energy storage in a fluidized bed of PCM. Chem Eng J 2013;230. https://doi.org/10.1016/j.cej.2013.06.112.